Fermi National Accelerator Laboratory

PION-PROTON BACKWARD ELASTIC SCATTERING BETWEEN 30 AND 90 GeV/c

W. F. Baker, D. P. Eartly, R. M. Kalbach, J. S. Klinger,
A. J. Lennox, P. A. Polakos, A. E. Pifer and R. Rubinstein

University of Arizona, Tucson, Arizona   85721

and

Fermi National Accelerator Laboratory
Batavia, Illinois   60510

November 1982

PION-PROTON BACKWARD ELASTIC SCATTERING BETWEEN 30 AND 90 GeV/c

W. F. Baker, D. P. Eartly, R. M. Kalbach,* J. S. Klinger,**
A. J. Lennox, P. A. Polakos,+ A. E. Pifer and R. Rubinstein

University of Arizona, Tucson, Arizona 85721

and

Fermi National Accelerator Laboratory
Batavia, Illinois 60510

ABSTRACT

Backward elastic scattering of $\pi^{\pm}$ on protons has been measured for incident pion momenta between 30 and 90 GeV/c and $0 < -u < 0.5$ $(GeV/c)^2$. The u-dependence of the cross sections is similar to that observed at lower momenta, and Regge models give acceptable fits to the data.

I. INTRODUCTION

This paper reports the final results of a Fermilab experiment designed to investigate πp elastic scattering in the range $0 \leq -u \leq 0.5$[1] [or $180^O \geq \theta_{\pi_{cms}} \geq 160^O$] for incident pion momenta P from 30 to 90 GeV/c. Preliminary results have already been reported[2].

Experimental interest in backward elastic scattering was stimulated in 1964 when a hydrogen bubble chamber group at CERN reported[3] the observation of an accumulation of elastic events near u = 0 with incident 4 GeV/c positive pions. Other experiments[3-11] followed, firmly establishing the existence of a sharp peak in the elastic cross section at u=0 for both π^+p and π^-p interactions with incident pion momenta from ~2 to 20 GeV/c.

The data below 20 GeV/c are found to have a natural division at ~5 GeV/c. Below this momentum, the differential cross section at u = 0 varies considerably with momentum showing several peaks and dips. The correlation of the momenta at which these phenomena occur with the masses of known baryon resonances supports the idea that a major contribution to the backward cross section comes from resonance (N* and Δ) formation in the s-channel, followed by decay of the resonance back to πp. Good fits to the data are obtained[9] for the scattering amplitude being the sum of a Breit-Wigner resonance amplitude and a non-resonant background, usually written in terms of a Regge amplitude.

Above 5 GeV/c, the resonance contribution subsides and up to 20 GeV/c the data show the following characteristic features:

1. The elastic differential cross section at u=0 for π^+p interactions is larger than for π^-p interactions. At 6 GeV/c, the ratio π^+/π^- is ~4.

2. The momentum dependence for the differential cross section at u=0 falls smoothly as P^{-n} (P is the laboratory momentum in GeV/c); values of n obtained are n = 2.0 for π^-p and n = 2.7 for π^+p scattering.

3. For fixed incident momentum, the dependence of the differential cross section $d\sigma/du$ on u near u = 0 is of the form e^{Bu}.

4. For π^+p scattering, a sharp dip in $d\sigma/du$ is observed near -u = 0.15. No such dip is observed for π^-p scattering.

Figure 1 shows some typical data existing prior to this experiment.

Although several optical models are capable of predicting peaks in the backward hemisphere[12,13], none can satisfactorily explain the observed differences in magnitude

and shape between π^+p and π^-p backward scattering. The best fits to the data were obtained with a model based on Reggeized baryon exchange.[15,16]

Typical baryon exchange diagrams for π^-p backward elastic scattering are shown in Figure 2. The scattering amplitude M for such a process in the Regge theory is written as:[17]

$$M = F(u)\frac{1 + i\tau e^{-i\pi\alpha(u)}}{\cos \pi\alpha(u)} \left(\frac{s}{s_o}\right)^{\alpha(u)-1/2}$$

where $F(u)$ - real function of u

$\alpha(u)$ - Regge trajectory

τ - ±1 signature of trajectory

s is the total energy in the cms

s_o is a constant

This gives a differential cross section of the form:

$$d\sigma/du \sim |\underline{M}|^2 = f(u)\left(\frac{s}{s}\right)\left(\frac{s}{s_o}\right)^{2\alpha(u)-2}$$

This expression leads to the prediction that $d\sigma/du$ for fixed u varies as a power of s; at high energies s is proportional to P so that $d\sigma/du$ varies as a power of P. We will make the conventional assumption of linear trajectories i.e. $\alpha(u) = \alpha(0) + \alpha'u$. This assumption is observed to hold in the positive u region of the Chew-Frautschi plot where the fit is to particle masses.

In general the Reggeized baryon exchange model allows for the exchange of the N_α, N_γ and Δ_δ trajectories in π^+p scattering and the exchange of only the Δ_δ trajectory in π^-p scattering. Experimental data indicate the dominance of the N_α trajectory in π^+p scattering. These data show the backward cross sections for π^-p (where only the Δ_δ trajectory is exchanged) to be appreciably smaller than for π^+p scattering up to the highest energies measured prior to this experiment. Since the Δ_δ contribution to the π^+p cross section is 1/9 its contribution to the π^-p cross section (due to Clebsch-Gordon coefficients) its contribution to the overall π^+p cross section is concluded to be small. The argument that the N_γ contribution is smaller than the N_α is based on the observation that in the region near $-u=0.15$ where the N_α amplitude vanishes, (see later) the π^+p cross section has a sharp dip. Since the N_γ amplitude is not

predicted to vanish there, the small value of the cross section at the bottom of the dip should reflect an upper limit on the N_γ contribution. Also, since the N_γ trajectory lies below the N_α , as determined from the Chew-Frautschi plots, the influence of the N_γ exchange should decrease with increasing momentum relative to N_α.

One striking prediction of the Regge models is the existence of the dip in π^+p backward scattering. The signature term $1 + i\tau e^{-i\pi\alpha(u)}$ for the N_α trajectory vanishes at $-u = 0.15$ (where $\alpha = -0.5$), and indeed the cross section becomes small at that u value, as seen in Figure 1. No corresponding dip is predicted in π^-p, and none is observed. Fits to $\pi^\pm p$ backward scattering with N_α and Δ_δ trajectories were carried out in the late 1960's, and good agreement reached; an example is shown in Figure 3. The trajectory parameters obtained were close to the Chew-Frautschi plot values.

Subsequent results from polarization experiments and from the reaction $\pi^-p \to n\pi^\circ$, which also may exchange N and Δ trajectories, could not be explained by this simple Regge model. More sophisticated models, incorporating additional trajectories, absorption and cuts, were proposed to fit the data.[18-20] However, for $\pi^\pm p$ scattering near u=0 it was believed that the simple model would remain approximately valid, and we later make comparisons between this model and our data.

Using this simple model, an important prediction for data above 20 GeV/c can be obtained. Since the N_α trajectory lies below the Δ_δ, the N_α amplitude falls more rapidly than the Δ_δ with increasing momentum, so that at high enough momentum both scatterings should be dominated by Δ_δ exchange. This leads to the prediction that the π^+p cross section at u=0 should become $\sim$ 1/9 that of $d\sigma^-/du$, contrary to the situation at lower momenta. The fit to low momentum results predicts the cross sections to cross at $\sim$50 GeV/c.[16,18,21] In addition, the dip in the π^+p angular distribution should disappear at high momentum, gradually being filled in by the contribution from the Δ_δ exchange. Eventually the π^+ angular distribution should become similar to that of π^-.

The first results above 20 GeV/c came from experiments performed at Serpukhov by Babaev et al[22,23] during the first half of the 1970's, where they studied the reactions $\pi^-n \to n\pi^-$ (isotopically equivalent to $\pi^+p \to p\pi^+$) and $\pi^-p \to p\pi^-$ at momenta near 25 and 40 GeV/c. For the former reaction, they measured $d\sigma^+/du$ at u=0 to be about a factor of 3 larger than was expected from an extrapolation of low momentum results using the expected $p^{-2.7}$ momentum dependence, although the angular distribution remained sharply peaked as at lower momenta. In the latter reaction, although the magnitude of the cross section $d\sigma^-/du$ at u=0 was consistent with Regge predictions, the angular distribution became much more

peaked near u=0. Some data are shown in Figure 4. These results could not be explained by the conventional Regge model. Models were proposed[24-26] which included the existence of new (non-Regge) terms in the scattering amplitude. The effect of such terms, it was argued, would not be seen at lower momenta, due to small couplings, but would have a lesser momentum dependence than Regge terms and would eventually dominate. The experiment described here was performed to test theoretical models to the highest momentum practical, and also to cover the momentum range of the Serpukhov experiments again. Its design was driven by the expectation that the cross sections to be measured would be small, of order nb/(GeV/c)^2.

II. EXPERIMENTAL METHOD

a. Introduction

Pions in a beam of known momentum and direction were elastically scattered off the protons in a liquid hydrogen target. The scattering angles and momenta of the recoil pions and protons were measured in separate magnetic spectrometers, each consisting of an analysis magnet with scintillation counter hodoscopes and multiwire proportional chambers (MWPC's) on either side to determine particle trajectories. One spectrometer ("forward"), downstream of the hydrogen target, recorded the forward scattered proton;

the second ("backward") was located just upstream of the hydrogen target to record the backward scattered pion. A threshold gas Cerenkov counter in the forward spectrometer identified the forward scattered particle as a proton. The scintillation counter hodoscopes provided a fast, although imprecise, momentum-angle measurement for each particle. An electronic comparison was made between the forward and backward hodoscopes, and any event whose correlation was close to that expected for an elastic scatter gave a trigger which caused the information from the MWPC's and other spectrometer instrumentation to be recorded on magnetic tape for off-line analysis. As will be described in Section IId, there were two different experimental layouts used for the forward spectrometer, in order to maintain resolution and acceptance over the incident momentum range from 30 to 90 GeV/c. The backward spectrometer was not changed during the experiment since the backward scattering kinematics are relatively independent of incident momentum. Figure 5 shows the experimental layout for 30 and 50 GeV/c data taking.

The experiment used beam for a total of 1500 hours including set-up time. A summary of the data acquired and analyzed during the experiment is given in Table 1. A more detailed description of the apparatus follows.

b.   Beam

This experiment used the M6 beam in the Meson Area at Fermilab.   The pions were produced by a 400 GeV proton beam from   the   Fermilab   Proton   Synchrotron   striking   a 30.5 x 0.15 x 0.15 cm beryllium target. Secondary particles produced at a 2.5 mr horizontal angle were collected, momentum analyzed and identified in a 420 meter long beam line, and directed onto the liquid hydrogen target.   A schematic layout of the beam transport components is shown in Figure 6, and a more complete description is available in Reference 27.

The beam contained three stages and three foci; each stage contained the sequence: point-to-parallel quadrupoles, dipole,   parallel-to-point   quadrupoles.   The   momentum acceptance of the beam was defined by a collimator at the first focus. During the experiment its aperture was varied to maintain the desired flux on the liquid hydrogen target.

Momentum dispersion at the second focus was 4.442cm per ($\%\Delta p/p$), and a momentum measuring scintillation counter hodoscope was placed at this location. For this experiment, a parallel beam at the liquid hydrogen target was desired, and so the final beam quadrupoles (Q14-17 in Figure 6) were not used.

Beam particles were recorded by two scintillation counters (B_1, B_2 in Figure 5), together with A, a halo veto counter with a hole for the beam to pass through.   The dimensions of all counters are given in Table 2.

Particle identification in the incident beam   was provided by an 18 meter long helium gas threshold Cerenkov counter C_π located in the third section of the beam line. With its pressure adjusted just above pion threshold, it eliminated triggers caused by protons or kaons.   The remaining muons and electrons were measured at every beam momentum and polarity.   The percentage of   muons   was determined by measuring beam transmission through a 4.5 meter iron beam stop, and varied between 1% and 2% depending on beam momentum. Electrons were measured with a lead glass shower counter, and varied from ~10% of the beam at 30 GeV/c to a negligible fraction above 70 GeV/c.

At the hydrogen target the beam size was approximately 3.8 cm in diameter, with a divergence of ~±0.3 milliradians and a nominal momentum spread of ±0.2%.   There   were approximately 1.5×10^6 beam pions per 1 second synchrotron spill. The pion beam had the accelerator RF time structure, and the pions arrived in "buckets," each separated by 18.8 ns; roughly 1 bucket in 35 was occupied by a beam particle.

A 32 element scintillation counter hodoscope was placed at the second focus (F2) to measure the relative momentum of each incident pion. Each element was 3mm   wide   and

overlapped its neighbor by one third giving a spatial resolution of 1mm; this corresponded to a momentum resolution of ±0.024%. The absolute value of the central momentum was set by means of a nuclear magnetic resonance apparatus installed in a beam dipole. Two sets of wire proportional chambers (W1 and W2 in Figures 5 and 7) located 22 and 3 meters respectively upstream of the liquid hydrogen target provided directional and positional information on each incident pion. Each set contained both x and y planes with wire spacings of 2mm.

c. Liquid Hydrogen Target

The target was a cylindrical vessel, 1 meter along the beam direction and 7.5 cm in diameter, constructed of 0.25mm mylar. The vessel was wrapped in ~40 layers of 6.4µm aluminized mylar thermal insulation in an evacuated outer vessel. The outer vessel had a large exit window constructed of 0.4mm mylar spanning the entire length of one side and the upstream face, to allow for the incoming beam and the large angular range of the outgoing scattered pions. Another window at the downstream end allowed the outgoing proton and the uninteracted beam to exit from the target. The target vessel was filled from a reservoir above the target which contained hydrogen liquified by a small helium refrigerator.

All sides of the target enclosure, excluding the windows, were covered by veto counters to improve rejection of inelastic interactions. Additional veto counters (some preceded by a thin lead sheet) were also located downstream of the target (see Figures 5 and 7).

d. Forward Spectrometer

Trajectory and momentum information on the forward going proton was provided by four sets of MWPC's located on either side of an analysis magnet as shown in Figure 5. The two chambers (W3,W4) located between the target and the magnet consisted of one x and y plane each; the two behind the magnet (W5,W6), one x plane each. Lateral wire spacing for all planes was 2mm and the chamber sizes were always such that they did not constitute aperture limits. Momentum measurement was by means of either one or two standard Fermilab BM109 analysis magnets. Each magnet had a gap of 6" x 24" and a pole length of 72".

In order that resolution and acceptance could be maintained over the desired momentum range from 30 to 90 GeV/c, two experimental layouts were used. In the first (shown in Figure 5), for data taking at ±30 and ±50 GeV/c, the overall spectrometer length was 30 meters with a single analysis magnet located 11 meters from the target; its magnetic field integral was 1337 kG-inch for both incident momenta, which provided a momentum resolution

$$\frac{\Delta P}{P^2} = \pm 2 \times 10^{-4} \ (GeV/c)^{-1}$$

The scattering angle resolution, $\Delta\theta$, of this arrangement was ±0.34 milliradians.

In the second layout, used for additional running at -50 GeV/c, and for running at ±70 and -90 GeV/c, the overall spectrometer length was increased to 60 meters. Two analysis magnets, located a distance of 31 meters from the target, were used to obtain the desired momentum resolution. Their magnetic field was scaled with momentum to provide the same resolution at each momentum, with a total field integral of 2546 kG-inch at 90 GeV/c. This geometry had momentum ($\Delta P/P$) and scattering angle resolutions of ±0.4% and ±0.110 mr respectively. For both layouts, the forward spectrometer acceptance for backward elastic scattering was well matched to that of the backward spectrometer.

The forward spectrometer contained two hodoscope planes of eight scintillation counters each, located downstream of the analysis magnet (F^α, F^β in Figure 5) to provide some determination of the scattering angle and momentum of the forward particle. The F^α counters were placed side by side, while those of the F^β hodoscope partially overlapped. The elements of each hodoscope were located such that a simple coincidence between a given element in F^α and the corresponding element in F^β signaled a particle of a scattering angle and momentum consistent with an elastic

scatter. The counter sizes are given in Table 2. The approximate resolution of a pair of elements was ~5 and ~3 mr for the low and high momentum geometries respectively, corresponding to a momentum resolution, $\frac{\Delta P}{P}$ = ±13%. The information from this telecope, together with that from the backward spectrometer hodoscope, provided the kinematic constraints in the trigger in order to heavily favor elastic scattering.

A 1.5 meter diameter, nine meter long nitrogen gas filled Cerenkov counter (C_F) was also located in the downstream part of the forward spectrometer. Its pressure was set just below the threshold of the highest momentum proton expected from an elastic scatter, to veto forward pions. The counter was most useful in the π^+ running, where an inelastically forward scattered π^+ often could closely resemble in kinematics the proton from a backward elastic scatter. In this case, the trigger rate was typically reduced a factor of 70 by including the Cerenkov counter in veto. For π^- running, a forward scattered π^- was deflected in the opposite direction by the analysis magnet from an elastically scattered proton, and the Cerenkov counter veto only reduced the trigger rate by 1.6 in this case.

The Cerenkov light produced in the counter was focused by four adjacent spherical mirrors mounted at the downstream end onto the 1.5" photocathode of an RCA 31000M photomultiplier. Particles leaving the counter had to

traverse the one-inch thick mirror glass so the counter was placed as close as possible to the final MWPC to minimize position measurement errors caused by multiple coulomb scattering and interactions in the glass.

e.   Backward Spectrometer

The backward spectrometer, shown in Figure 7, was on an axis 135° to the incident beam direction; this angle was determined by a Monte Carlo program to provide the largest geometrical acceptance for the given magnet aperture. Since the backward scattered pion kinematics are relatively independent of incident momentum in the range covered by this experiment, the same layout and spectrometer magnetic field could be used for all momenta, eliminating many instrumental uncertainties.

MWPC's were used to define particle trajectories on either side of the analysis magnet. Upstream of the magnet, horizontal track position was determined by 2 planes of vertical wires with 2mm spacing, separated by 13cm; vertical position by 3 planes of horizontal wires also with 2mm spacing and separated by 13cm and 10cm. The chambers were aligned and fixed in a cradle attached to the front face of the magnet; this compact configuration permitted close placement of the analysis magnet to the target in order to maximize acceptance. The analysis magnet aperture was 183cm x 46cm with a pole length of 46cm; its central field was 4.2

kG with an effective field integral of 126 kG-inches. The magnetic field polarity depended on incoming pion polarity and was such that the backward elastically scattered pion was always bent away from the incident beam. An incident beam channel in the magnet return iron allowed the magnet to be positioned to maximize the pion scattering angle acceptance. The field in this channel introduced a slight deflection in the incident beam direction which was measured during calibration runs and corrected in the analysis. Behind the magnet, only the horizontal track projection was measured, using two planes of vertical wires. Wire spacing in the planes was 2mm with adjacent wires joined together, yielding an effective spacing of 4mm. The distance between planes was ∼40cm. To accommodate the large angular range of the backward scattered pions in the laboratory, these planes each consisted of several individual chambers positioned side by side; two in the first plane, three in the second. The chamber frames were overlapped to minimize holes in the acceptance. Monte Carlo calculation showed this effect to be smeared in u due to the finite target length and the acceptance was corrected accordingly. The sensitive areas of all wire planes were sufficiently large that they were not aperture limits.

Located behind the final MWPC plane was a hodoscope $(S_1-S_{12}$ in Figures 5 and 7). It consisted of 24 scintillation counters 11" wide x 12" high in a 2 high by 12

wide array. The pion position measured by this hodoscope gave approximate information on the pion momentum and scattering angle (assuming it to be elastic). This information was then used with that from the forward spectrometer telescope in making the trigger decision. A single counter near the target (S_o in Figure 7) was put in coincidence with most of the S counters to help eliminate background triggers from particles not coming from the hydrogen target. The time between beam arrival and the signal in a particular hodoscope element was measured using time-to-digital converters (TDC's) and recorded for each event. This information proved useful in the off-line analysis in eliminating those remaining accidental triggers not originating in the target.

f. Fast Logic

The fast logic system rapidly identified events where the trajectories of both particles from the hydrogen target were consistent with those expected for an elastic event. A simplified block diagram is given in Figure 8.

A beam pion was identified by the coincidence $B=B_1B_2AC_\pi$. To minimize background in the MWPC's, a beam pion was accepted only if it was not accompanied by a second beam particle within ±25 ns. A signal from an element of the S-hodoscope at the correct time following B_2 defined as $BS=B.S_o.(S_1+S_2+...S_{12})$, indicated that a particle had

emerged from the target and passed through the backward arm. (S_o was only used for channels S_3-S_{12}). The BS signal was used as a pretrigger which temporarily disabled the experiment and stored the MWPC and S-hodoscope information in latches until the signals from the forward hodoscopes and Cerenkov counter were received and processed. Typically 1 beam pion in 2000 resulted in a BS pretrigger. The individual coincidences BS_oS_i were also formed and sent to delay lines for later use in forming the final trigger.

Following a delay of ~400ns, the forward hodoscope signals were received and the coincidences $F_i = F_i^\alpha . F_i^\beta$ (i=1,8) were formed. At this point, the kinematic constraints were imposed. The signal BSF, defined as:

$$BSF = \Sigma \ BS_iA_{ij}F_j \qquad i = 1,12; \ j = 1,8$$
$$\text{where } A_{ij} = 8x12 \text{ matrix of 0's and 1's}$$

was formed in a hard-wired coincidence matrix using commercial fan-ins, fan-outs and coincidence circuits. This matrix contained all of the correlations between elements of the forward and backward hodoscopes for backward elastic events; the correlations were determined by Monte Carlo simulation of elastic events in the apparatus, and changed with incident momentum. A BSF signal thus indicated that an event had a hodoscope hit pattern consistent with that expected for an elastic event, although such patterns could also occur from inelastic scatters whose kinematics were close to elastic, and from interactions occurring upstream

of the liquid hydrogen target. The latter source was dominant.

The final coincidence, MASTER TRIGGER = $BSF.\bar{C}_p$ insured that the forward particle was a proton. This caused a readout cycle transferring the event data stored in the latches, TDC's and scalers to the computer memory and eventually to magnetic tape. Upon completion of the transfer, the TDC's, latches, and appropriate scalers were reset and the experiment restarted. An entire event cycle took approximately 10 milliseconds.

Any BS pretrigger which was not followed by the appropriate signals from the forward counters resulted in the clearing of all temporarily stored data and the prompt reenabling of the experiment without computer readout. The deadtime thus introduced was $\leq$ 2 μsec. Approximately 99% of the pretriggers fell into this category. Table 3 gives some typical rates during the experiment.

A random selection of events triggered by beam only, and also by BS only, was recorded continuously throughout the data-taking. The total number of pions, as defined by the beam telescope, incident on the liquid hydrogen target during the time the experiment was enabled was scaled at each momentum and used to normalize the final differential cross sections.

g. PWC's

The PWC's were each constructed of two sets of wire planes built on aluminum reinforced G10 frames. Anode (signal) wires were 0.025 mm gold-plated tungsten, and cathode wires were 0.076 mm silver-clad beryllium-copper. The gap between anode and cathode was 5.4 mm. The gas was a mixture of 80% argon, 19.9% CO_2 and 0.1% freon 13B1. Typical operating voltages were 4-4.5 KV.

The readout system was based upon the Nevis Laboratory design of Sippach[28] and used amplifier/discriminator cards mounted on the PWC's feeding long stripline delay cables. These cables in turn fed into coincidence registers (located in the experiment counting area) which were gated by signals from the fast logic. The PWC's contained a total of 4300 wires.

III.   DATA ANALYSIS

a.   Introduction

The data from the experiment were analyzed on the Fermilab CDC-6600 computers. The analysis procedure for each event included the geometrical reconstruction, during which many obviously non-elastic events were excluded, followed by the calculation of several kinematic variables which were a measure of how near to elastic the event was. Elastic events were finally selected by making the

appropriate cuts on these kinematic variables. Since the cross sections (and hence statistics) were small, particular attention was given to making the analysis program as efficient as possible in extracting elastic events from the data.

b. Reconstruction

The first stage of the analysis began with the geometrical reconstruction in the backward spectrometer. Tracks were first reconstructed in the horizontal (x) projection in front of and behind the analysis magnet. For this to be possible, at least 3 of the 4 MWPC x planes in the backward arm had to record at least one hit. From the measured efficiencies of the chambers, >95% of the pions from elastic interactions had trajectories which could be reconstructed. Events were divided into two groups: those in which all 4 x-planes recorded at least one hit, and those in which only 3 of 4 x-planes recorded hits.

For events in the first group, a track was formed by joining with a straight line a hit in one x-plane with a hit in the other on the same side of the analysis magnet; if planes had more than one hit, all combinations were used to produce a set of tracks. This procedure was used to reconstruct tracks on both sides of the analysis magnet. To reduce the number of tracks which did not correspond to true charged particle trajectories, a track behind the analysis

magnet was accepted only if it extrapolated to an S-hodoscope element which had recorded a hit. If no track was accepted, it was assumed that one of the planes failed to record a true hit but contained spurious accidental hits. The event was then reclassified into the second group.

For events with only two hits on one side of the magnet and one on the other, tracks from the two-hit side were traced through the magnetic field to the hit on the opposite side by varying the curvature (momentum) of the track in the field region. All possible combinations were tried and again only those tracks behind the magnet which extrapolated to an S-hodoscope element which was hit were considered valid.

Either procedure described above produced two sets of tracks, one before and one after the magnet. Tracks from each set were paired with the requirement that they meet within the magnet volume, and the momentum was calculated. The event was required to have a track that pointed back to the liquid hydrogen target, and had the correct sign momentum. The TDC information was used to insure that it had the proper time of flight from the target to the S-hodoscope for an elastic pion.

Tracks were reconstructed in the vertical (y) projections before the magnet, with the requirement of hits in at least two of the three chambers. Events meeting all of the criteria described so far were recorded on a data

summary tape for further analysis. This first stage analysis eliminated ∼ 90% of the raw triggers.

In the second stage of the analysis, incident beam tracks and tracks in the forward spectrometer were reconstructed in both x and y projections. For the beam tracks, information from both beam chambers was used unless there was no W1 chamber hit due to inefficiency. In the latter case position information from the W2 chamber was used and the nominal beam direction was assigned to the track. Due to the small divergence of the beam, this procedure introduced negligible error. A hit in W2 was always required. Each beam track was extrapolated through the channel in the backward spectrometer magnet, taking into account the fringe field in the channel. It was then paired with a reconstructed track from the backward spectrometer, and the target vertex coordinates as well as the x and y projections of the backward pion scattering angle were calculated.

For the forward arm upstream of the analysis magnet, tracks in the x projection were reconstructed using W4 and the target vertex. W3 was not required but was included in the fit if it had a hit. In the event that there was no hit in W4, the track was constructed using a hit in W5 and extrapolating back through the magnet to the target vertex assuming its momentum to be elastic. Thus, the existence of a valid forward track and the horizontal projection of the

proton scattering angle, θ_x^P, were determined by requiring only a hit either W4 or W5. The vertical projection of the angle, θ_y^P, was calculated using the target vertex and either W4 or W3. This procedure for determining the proton scattering angle minimized the number of events lost because of possible chamber inefficiencies. A kinematics program used the incident pion momentum and the backward scattering angle, θ^π, to predict the momenta of the backward pion and forward proton, P_π' and P_p'. The proton trajectory downstream of the analysis magnet was calculated using P_p' and the reconstructed proton track between the target and the analysis magnet. The event was rejected if the trajectory did not intersect the hodoscope elements in F^α and F^β which were involved in the trigger.

In anticipation of cuts which would be applied later, the variables x_π, ΔP_x, ΔPy and ΔX_{W6} were calculated and recorded during the second stage of analysis. The first quantity is defined as

$$x_\pi = \frac{P_\pi - P_\pi'}{P_\pi \cdot P_\pi'}$$

and measures the discrepancy between the measured and predicted scattered pion momentum. It has the property that the width of the distribution of elastic events in x_π is constant for all scattered pion momenta, allowing the final elastic cut on this variable to be the same for all

scattering angles. The second and third quantities are transverse momentum imbalances defined by

$$\Delta P_{x,y} = P^{\pi}_{x,y} - P^{P}_{x,y}$$

where $P^{\pi}_{x,y} = P'_{\pi} \sin \theta^{\pi}_{x,y}$ and $P^{P}_{x,y} = P'_{p} \sin \theta^{P}_{x,y}$. The fourth quantity Δx_{W6} is the distance between the predicted intersection of a proton trajectory with W6 and the closest recorded hit in W6.

c.   Event Selection

After the events were reconstructed, histograms were made of the number of events versus the variables x_{π}, ΔP_x, ΔP_y and Δx_{W6}. Examples are shown in Figures 9-12. In these Figures, the unshaded histograms show the number of events before any kinematic cuts were applied. These plots all showed the same characteristic feature of a sharp peak about the (expected) value zero, containing the elastic events, superimposed on a rather smooth background of inelastic events. In the histogram of x_{π}, shown in Figure 9, the inelastic background, as expected, is mostly to one side of the peak, since the momentum of an inelastically scattered pion is always less than that of an elastically scattered pion at the same angle. The width of the peak directly reflects the momentum resolution of the backward spectrometer.

The final selection of elastic events was made by choosing those events which fell within a prescribed interval about the elastic peak in each of the 4 variables. The limits of this interval for a given variable were determined by observing the width of the elastic peak in the variable after all of the other cuts were made. The shaded histrograms in Figures 9-12 show the number of events remaining after the cuts on all variables except the one plotted.

The events accepted by the elastic cuts were used to generate a final histogram of the number of events versus u, with the value of u for each event calculated from the scattering angle of the backward pion. Events in this histogram consisted of the true elastic scatters together with a small background of inelastic events under the elastic peak.

d.   Inelastic Background

Inelastic background in the final data sample was calculated using the distribution of events in the variable x_{π}. From a histogram similar to the lower curve of Figure 9 (the distribution of events surviving the elastic cuts on all the variables except x_{π}), the background outside the elastic peak was found to be approximately flat for positive x_{π}, and to eventually fall to zero for negative x_{π}. To determine the amount of background beneath the elastic peak,

the assumption was made that it varied linearly from its level on one side of the elastic peak to its level on the other. A ±50% systematic error in the background was included to allow for uncertainty in this procedure. The distribution of inelastic events in u was then determined by histograming the u values of events which satisfied the elastic cuts on all variables except x_π. Assuming the inelastic events beneath the elastic peak had a similar distribution in u, a subtraction of the background could then be made. Since the statistics in this histogram were generally poor, fluctuations of the background level in u were smoothed out using a simple fit. Some checks of these procedures were made by selecting inelastic events from outside the elastic peak. Within limited statistics, they were shown to be correct.

For the π^- data, the background subtraction was always less than 10% at 30, 50, and 70 GeV/c, but increased to ⌁25% at 90 GeV/c for $-u \geq 0.25$. For π^+, at 30 and 50 GeV/c and near u=0 for 70 GeV/c, the subtraction again never exceeded 10%. However, at 70 GeV/c, in the region of the dip and beyond $(-u \geq 0.5)$ the background became equal to the signal. In this region, only upper limits are quoted for the cross section.

Quasi-two-body reactions such as $\pi p \to N^* \pi$, $N^* \to p \pi^\circ$ and $\pi p \to N \rho$, $\rho \to \pi \pi^\circ$ may not be correctly subtracted by the process described above. However, a Monte Carlo study showed that

under 1% of such reactions would have decay charged particles falling within our analysis cuts. Around 10 GeV/c, these reactions have cross sections similar to elastic scattering,[29,30] and since they are also baryon exchange processes, we would expect this to be also true for momenta between 30 and 90 GeV/c. They should therefore contribute a negligible background to our data.

e.   Corrections and Acceptance

The measured cross sections were corrected for muons and electrons in the pion beam (1.5-12.7%); more than one beam particle in an rf "bucket" (2%); absorption in the hydrogen target, air, Cerenkov counter mirrors, MWPC's, and counters (⌁30%); and accidental vetos of elastic events by delta rays produced in the target (4.9%).

The geometrical acceptance of the apparatus at each incident momentum was determined by a Monte Carlo program. Elastic events were generated in the hydrogen target and the scattered particles propagated through the spectrometer arms with multiple scattering included; measured incident beam parameters (momentum spread, divergence and spot size) were used. The probability of detecting an event was calculated as a function of u. The 30 GeV/c acceptance curve is shown in Figure 13; curves for the other incident momenta are similar. Because the overall acceptance was essentially determined by the fixed vertical acceptance of the

S-hodoscope counters, the acceptance curve exhibits an approximate $(\sin \theta^\pi_{lab})^{-1}$ dependence expected for this type of geometrical constraint.

MWPC efficiencies, measured during special calibration runs at various times during the data taking, varied between 85-98% depending on the chamber. Chamber response as a function of time was very stable.

The efficiency of the analysis program for identifying elastic events as a function of u was measured using Monte Carlo generated events. Included in the event generating procedure were the effects of MWPC spatial resolution, MWPC efficiency, multiple coulomb scattering, incident beam phase space and scattered pion decay. To account for the effect of the additional random background hits present in the MWPC's and hodoscopes, real data taken at random times during the beam spill were added to the Monte Carlo generated elastic MWPC and hodoscope data. The resulting events were then processed by the analysis program. Including the effects mentioned above, between 78-86% of the elastic events were identified as such. Most of the events that were not identified as elastic lacked sufficient MWPC data due to the measured chamber efficiencies included in the program. If the chambers had been 100% efficient, the program would have identified >98% of the Monte Carlo events as being elastic.

Radiative corrections were calculated using the procedure outlined in References 31-34. For π^+p scattering, the correction was negligible; for π^-p the correction changed the overall normalization of the differential cross sections by a factor 1.14-1.18 depending on momentum. The correction was independent of scattering angle.

Several runs were taken with the target empty to determine the contribution from events not originating in the liquid hydrogen. It was found to be negligible.

IV. RESULTS

The results are presented in tabular form in Tables 4 and 5, and graphically in Figures 14 and 15 (together with some earlier results). The errors quoted are statistical and represent one standard deviation. For those bins in which no signal above background was found, the cross sections are given as upper limits and represent 90% confidence levels. Because of uncertainties in the previously discussed corrections, the uncertainty in the overall normalization of the cross sections is estimated to be ±15%.

a.   General Features

1)   The u distributions of the cross sections $d\sigma/du$ for both π^+ and π^- we have measured at 30 GeV/c and above are similar to those previously obtained below 20 GeV/c. In

Figures 14 and 15, the results may be compared with the π^+ results of Baker et al.[8] at 7 GeV/c and the π^- results of Owen et al.[7] at 6 GeV/c. For π^+p scattering the steep backward peak and the dip at $-u=0.15$ as well as the broad second maximum between $-u=0.15$ and 0.45 are all present, at least up to 50 GeV/c. The data at 70 GeV/c are also consistent with these features.

2) In the region of the backward peak, the cross section has an approximately exponential dependence on u. The data in the region $-u\leq0.1$ for positive pion scattering and $-u\leq0.5$ for negative pion scattering were fit using the relation $d\sigma/du = Ae^{Bu}$. The fitted values for A and B are given in Table 6. The values of B range from 21 to 26 $(GeV/c)^{-2}$ for positive pion scattering and from 4 to 7 $(GeV/c)^{-2}$ for negative pion scattering. These are compared with the values of B obtained at lower momenta in Figure 16. For both polarities, they are consistent with a slow increase in B for incident momenta between 5 and 90 GeV/c.

3) The cross section $d\sigma/du$ at $u=0$ for π^+p is greater than for π^-p at all measured momenta. The ratio of π^+p/π^-p is 1.9 ± 0.3 at 30 GeV/c, 1.3 ± 0.3 at 50 GeV/c, and 1.5 ± 0.8 at 70 GeV/c.

4) The cross section $d\sigma/du$ at $u=0$, for both positive and negative pions, decreases with increasing momentum. The available data above 5 GeV/c including our own have been fit to the form:

$$\frac{d\sigma}{du}(P, u=0) = AP^{-n}$$

For the fits, the quoted statistical and systematic errors were added in quadrature for each experiment. For π^+, the data from Babaev et al.[22] at 23 and 38 GeV/c were not included in the fits (for reasons explained below). The results are shown in Figure 17. We obtain the values $n^+=2.31 \pm 0.07$ and $n^-=2.08 \pm 0.06$ with chi-squared probabilities of 26% and 21% respectively. Fits to the data of this experiment only yield the values $n^+=2.51 \pm 0.36$ and $n^-=2.11 \pm 0.21$. Within errors, the two sets of results are consistent.

5) The data do not confirm the large values of $d\sigma/du$ at $u=0$ for π^+p scattering, nor the large values of the π^-p slope parameter B observed in the data of Babaev et al.[22,23] As shown in Figure 17, their 40 GeV/c π^+p result is approximately 2.5 times larger than that expected from a smooth interpolation between the measurements of this experiment at 30 and 50 GeV/c. The angular distributions however are quite similar (see Figure 15). For π^-p scattering, the two experiments observe substantially different angular distribution as shown in Figure 14, where the 38 GeV/c Babaev et al[23] results have been included for comparison. Fits by the Serpukhov group to their data yield values for the parameter B of 23 and 19 $(GeV/c)^{-2}$ at 25 and 38 GeV/c respectively in comparison to the values of B

between 4 and 7 $(GeV/c)^{-2}$ for this experiment (see Figure 16). It should be pointed out that their data covered a much narrower u range than ours, hence their fits were limited to the region very close to u=0. The possibility that a real physics effect near u=0 leads to a sharp peak in the π^- distribution cannot entirely be ruled out. However our data, particularly at 50 GeV/c, do not support this hypothesis. Statistically, the Babaev et al. values of B are ∼2 - 2.5 standard deviations from the values expected by interpolation from other data, as seen in Figure 16.

b. Discussion

As was mentioned in the Introduction, many of the features of both π^+p and π^-p backward elastic scattering between the resonance region and 20 GeV/c can be explained by a simple Reggeized baryon exchange model using only the N_α and Δ_δ trajectories. We find the same to be true for the data obtained by this experiment between 30 and 90 GeV/c. In the model, the dip in the π^+p differential cross section at -u = 0.15 occurs because the amplitude of the N_α trajectory, assumed to dominate this process, vanishes at this u value. Since in π^-p scattering, the exchange of the nucleon trajectory cannot occur, a dip is neither expected nor seen at this u value.

The model also predicts the width of the backward peaks to slowly decrease with increasing momentum. Since experimentally the backward peaks at all energies may be parameterized by the form Ae^{Bu}, the parameter B should increase with increasing momentum P as B=2ln(P) + constant. The data above 5 GeV/c including those of this experiment, as shown in Figure 16, are consistent with this form.

The Regge model prediction that the cross section dσ/du for any value of u varies with increasing momentum as $s^{2\alpha(u)-2}$, where s is the CMS energy squared and α(u) is the trajectory of the exchanged Reggeon, can be used to derive effective Regge trajectories. These can be compared with the Δ_δ and the N_α trajectories which are assumed to dominate π^- and π^+ scattering respectively, as a check of the validity of this simple model. The available π^- and π^+ backward elastic data above 5 GeV/c including those of this experiment (and also the data of this experiment alone) have been fitted using this parameterization for several values of u in the range 0<-u<0.5 $(GeV/c)^2$. The chi-squared probabilities of the fits, which vary from 50% to 5% and from 70% to 10% as -u increases from 0 to 0.5 for π^+ and π^- scattering respectively, are an indication that this parameterization describes the data well. In the fitting procedure, a 15% systematic error was added to the quoted statistical error of each experiment to allow for uncertainty in the absolute normalization of the different

experiments. The results of the fits, expressed in terms of $\alpha(u)$, are shown in Figures 18 and 19 for π^- and π^+ scattering respectively.

For π^-p scattering, a linear least squares fit to the effective trajectory gives $\alpha(u)=-(0.06\pm0.05) + (0.50\pm0.26)u$ for the 5-90 GeV/c data, and $\alpha(u)=-(0.11\pm0.14) + (0.67\pm1.04)u$ for fits to the 30-90 GeV/c data of this experiment only. These results are consistent with the form of the Δ_δ trajectory, $\alpha(u)=0.0 + 0.9u$, obtained from Regge fits at lower energies.[18,19] The u=0 intercept of the effective trajectory gives the momentum dependence of the cross section $d\sigma/du$ at u=0 of $p^{2\alpha(0)-2} \simeq p^{-2.12}$, close to the $p^{-2.0}$ predicted by the model.

For π^+p scattering, we find the linear fit to the effective trajectory of the 5-70 GeV/c data (omitting Reference 22 as discussed earlier), $\alpha(u)=-(0.15\pm0.06) + (2.24\pm0.25)u$, to be somewhat steeper in u than expected for the N_α trajectory, which from low energy Regge fits is parameterized as $\alpha(u)=-0.37 + 0.9u$.[18,19] However, we find the effective trajectory derived in the range 30-70 GeV/c from the data of this experiment only, $\alpha(u)=-(0.37\pm0.11) + (0.58\pm0.50)u$, to be in better agreement. The higher u=0 intercept of the effective trajectory from the 5-70 GeV/c data, $\alpha(u)=-0.15$, gives a momentum dependence for $d\sigma/du$ at u=0 of $p^{-2.31}$ as opposed to the $p^{-2.7}$ dependence predicted by the model. If we use this $p^{-2.31}$ parameterization for

extrapolation, the prediction for the momentum at which the π^- cross section becomes larger than π^+ becomes $\sim$400 GeV/c.

For both π^+ and π^-, the observed shape of the u distributions are in reasonable agreement with predictions made several years ago from the simple Regge model[18]; this is illustrated in Figure 20 for our 50 GeV/c data.

c. Phenomenological Regge Model Fit

Since publication of our preliminary data,[2] an analysis of all backward scattering results including ours has been carried out by Mir and Storrow[35] based upon their earlier analyses using data up to 20 GeV/c.[19] In particular they examined the consistency of the lower momentum results upon which the predictions to higher momenta are based. They also included polarization data in their fitting.

As has been noted in the literature over the past several years, there are disagreements in the absolute normalizations quoted for the different experiments below 20 GeV/c. This leads to disagreements in the predictions for higher momenta, since the parameters of the model will vary according to which low momentum data are used.

Their model has three Regge exchanges, with the N_γ added to the two we have discussed earlier. The three trajectories are

$$N_\alpha: \quad \alpha(u) = -0.37 + 0.90u$$

N_γ: $= -0.43 + 0.90u$

Δ_δ: $= 0.90u$

In addition, the Δ_δ trajectory is modified from the standard Regge model by allowing the real and imaginary parts to have separate parameterizations.

Mir and Storrow allow the relative normalizations of the lower momentum experiments to float. In fitting to all of the data (both low momenta and ours), they find that normalization of lower momentum data to Anderson et al[6] does not give good fits. There is a slight preference for normalization to Baker et al[8] rather than to Owen et al,[7] and the χ^2 of the fits improve if the π^+ data of Owen at al are omitted from the fits. Examples of their fits to our data, using the Baker et al[8] normalization, are shown in Figures 21 and 22, and it can be seen that this model provides good fits. The Babaev et al[23] π^-p data is not ruled out, although the large values of B they quote are 2-2.5 standard deviations above values consistent with all other data. The $\pi^-n \rightarrow \pi^-n$ data of Babaev et al[22] are rejected as inconsistent with all other $\pi^+p \rightarrow \pi^+p$ data, as we have noted earlier.

V. CONCLUSIONS

We have measured π^+p backward elastic scattering between 30 and 90 GeV/c. The data show that features of this process observed at lower momenta continue to be present in this new momentum range. Among the observations are:

(i) $d\sigma/du$ has an exponential shape near $u=0$ for both π^+p and π^-p.

(ii) $d\sigma/du$ at $u=0$ falls as P^{-n} for both π^+p and π^-p.

(iii) The dip in $d\sigma/du$ for π^+p at $-u \sim 0.15$ is still present at high momenta.

(iv) Data from Serpukhov on $\pi^-n \rightarrow \pi^-n$ (isotopically equivalent to $\pi^+p \rightarrow \pi^+p$) at ~ 25 and 40 GeV/c are inconsistent with our data and all other π^+p data. Their values of the exponential slope for π^-p scattering are 2-2.5 standard deviations higher than consistent with other data.

(v) Regge models are able to fit the new data. We have shown simple Regge fits to previous data and the new data presented here. We have commented on a more comprehensive analysis carried out which includes our data; while some (not unexpected) modifications have to be made to the simplest Regge ideas, in general the results provide support to the Regge model.

ACKNOWLEDGEMENTS

REFERENCES

*   Deceased

** Present Address:

    Fairchild Republic, Farmingdale, New York, 11735

+   Present Address:

    Max-Planck Institute, Munich, Germany

1. u is the four momentum transfer squared, given by the expression $u = -2q^2(1+ \cos\theta_{cms})$; q = cms momentum, θ_{cms} = pion cms scattering angle. The units for u in this paper are $(GeV/c)^2$.

2. W.F. Baker, D.P. Eartly, R.M. Kalbach, J.S. Klinger, A.J. Lennox, P.A. Polakos, A.E. Pifer, R. Rubinstein, Phys. Rev. Lett. 43, 1635 (1979).

3. Aachen – Berlin – Birmingham – Bonn – Hamburg – London (I.C.) – Munchen Collaboration, Phys. Lett. 10, 248 (1964).

4. J. Orear, R. Rubinstein, D.B. Scarl, D.H. White, A.D. Krisch, W.R. Frisken, A.L. Read, H. Ruderman, Phys. Rev. 152, 1162 (1966).

5. H. Brody, R. Lanza, R. Marshall, J. Niederer, W. Selove, M. Shochet, R. VanBerg, Phys. Rev. Lett. 16, 828, 968(E) (1966).

6. E.W. Anderson, E.J. Bleser, H.R. Blieden, G.B. Collins, D. Garelick, J. Menes, F. Turkot, D. Birnbaum, R.M. Edelstein, N.C. Hein, T.J. McMahon J. Mucci, J. Russ, Phys. Rev. Lett. 20, 1529 (1968).

7. D.P. Owen, F.C. Peterson, J. Orear, A.L. Read, D.G. Ryan, D.H. White, A. Ashmore, C.J.S. Damerell, W.R. Frisken, R. Rubinstein, Phys. Rev. 181, 1794 (1969).

8. W.F. Baker, K. Berkelman, P.J. Carlson, G.P. Fisher, P. Fleury, D. Hartill, R. Kalbach, A. Lundby, S. Mukhin, R. Nierhaus, K.P. Pretzl, J. Woulds, Nucl. Phys. B25, 385 (1971).

9. A.J. Lennox, J.A. Poirier, C.A. Rey, O.R. Sander, W.F. Baker, D.P. Eartly, K.P. Pretzl, S.M. Pruss, A.A. Wehmann, P. Koehler, Phys. Rev. D 11, 1777 (1975).

10. A. Jacholkowski, B. Bouquet, B. D'Almagne, A. Ferrer, A. Lahellec, P. Petroff, F. Richard, P. Roudeau, J. Six, D. Treille, P. Rivet, P. Benkheiri, P. Fleury, G. De Rosny, A. Rouge, H. Yoshida, Nucl. Phys. B126, 1 (1977).

11. N.A. Stein, R.M. Edelstein, D.R. Green, H.J. Halpern, E.J. Makuchowski, J.S. Russ, D.M. Weintraub, Z. Bar-Yam, J.P. Dowd, W. Kern, J.J. Russell, N. Sharfman, M.N. Singer, Phys. Rev. Lett. 39, 378 (1977).

12. N. Sharfman, Z. Bar-Yam, J.P. Dowd, W. Kern, J.J. Russell, M.N. Singer, R.M. Edelstein, D.R. Green, H.J. Halpern, E.J. Makuchowski, J.S. Russ, N.A. Stein, Phys. Rev. Lett. 40, 681 (1978).

13. L.M. Simmons, Phys. Rev. Lett. 12, 229 (1964).

14. M. Derrick, CERN Report No. 68-7, Vol. I, p111. (1968). (unpublished)

15. C.B. Chiu, J.D. Stack, Phys. Rev. 153, 1575 (1967).

16. V. Barger, D. Cline, Phys. Rev. Lett. 21, 392 (1968).

17. V. Barger, D. Cline, Phys. Rev. 155, 1792 (1967).

18. E.L. Berger, G.F. Fox, Nucl. Phys. B26, 1 (1971).

19. J.K. Storrow, G.A. Winbow, Nucl. Phys. B53, 62 (1973); Nucl. Phys. B54, 560 (1973); J. Phys. G. 1, 263 (1975).

20. A.C. Irving, R.P. Worden, Phys. Rep. 34, 117 (1977).

21. E. Leader, Nature 271, 213 (1978).

22. A. Babaev, E. Brakhman, G. Eliseev, A. Ermilov, Yu. Galaktionov, Yu. Gorodkov, V. Kirilyuk, N. Luzhetsky, V. Lyubimov, V. Nagovitzin, V. Nozik, V. Pogidaev, V. Shepelev, E. Shumilov, I. Sidorov, I. Tikhomirov, T. Tsvetkova, O. Zeldovich, Phys. Lett. 38B, 342 (1972).

23. A. Babaev, E. Brakhman, M. Danilov, G. Eliseev, A. Ermilov, Yu. Galaktionov, Yu. Gorodkov, L. Laptin, V. Lyubimov, V. Nagovitzin, V. Plyaskin, V. Shepelev, E. Shumilov, V. Sopov, I. Tikhomirov, T. Tsvetkova, O. Zeldovich, Phys. Lett. 67B, 351 (1977).

24. I.F. Ginzburg, L.I. Perlovskii, Sov. J. Nucl. Phys. 17, 675 (1973), and 23, 120 (1976).

25. B. Diu, P. Tchang, Nuovo Cimento 32A, 185 (1976).

26. V.A. Lyubimov, Sov. Phys. Usp. 20, 691 (1977).

27. J.R. Orr, A.L. Read, Meson Laboratory preliminary design report, Fermilab 1971.

28. H. Cunitz, W. Sippach and J. Dieperink, Nucl. Instr. and Meth. 91, 211 (1971).

29. A. Rouge, G. De Rosny, P. Fleury, B. Eisenstein, P. Briandet, P. Benkheiri, P. Rivet, A. Volte, B. Bouquet, B. D'Almagne, A. Ferrer, A. Jacholkowski, P. Petroff, F. Richard, P. Roudeau, J. Six, D. Treille, H. Yoshida, Phys. Lett. 69B, 115 (1977).

30. P. Benkheiri, B. Eisenstein, P. Fleury, G. De Rosny, A. Rouge, J.M. Thenard, H. Yoshida, D. Treille, P. Rivet, A. Volte, B. Bouquet, B. D'Almagne, A. Ferrer, A. Jacholkowski, P. Petroff, F. Richard, P. Roudeau, J. Six, Lett. al. Nuov Cim. 20, 297 (1977).

31. M.R. Sogard, Phys. Rev. D9, 1486 (1974).

32. E. Borie, Z. Naturforsch 33a, 1436 (1978).

33. I.F. Ginzburg, G.L. Kotkin, V.G. Serbo, Phys. Lett. 80B, 101 (1978).

34. J.S. Klinger, Fermilab-Pub.-80/26-Exp (1980) (unpublished).

35. K.L. Mir and J.K. Storrow, J. Phys. G. 7, 1187 (1981).

TABLE 1.

Summary of Data Taken

Incident Particle	Momentum (GeV/c)	Pions on Target	Event Triggers	Elastic Events
π^+	30	25.5×10^9	130×10^3	100
π^+	50	45.4×10^9	263×10^3	62
π^+	70	49.6×10^9	621×10^3	14
π^-	30	33.7×10^9	256×10^3	142
π^-	50	88.6×10^9	271×10^3	121
π^-	70	58.3×10^9	305×10^3	31
π^-	90	43.0×10^9	233×10^3	13

TABLE 2.

Scintillation Counter Dimensions

Horizontal x vertical. Typical sizes for hodoscope elements are given when not all identical.

B_1, B_2	2" diameter circular
A	5.5" x 5.5" with 2" diameter circular hole
S_i	11" x 12"
F^α	2.75" x 7.5"
F^β	9.38" x 14.5"

TABLE 3.

Typical rates during the experiment

Beam pions per accelerator cycle	1.5×10^6
BS pretriggers per accelerator cycle	750
Master triggers per accelerator cycle	10
Elastic events per accelerator cycle	$2 \times 10^{-4} - 8 \times 10^{-3}$

TABLE 4.

Differential Cross Sections

$\pi^- p \rightarrow p \pi^-$

Statistical errors only are listed; there is an additional overall normalization uncertainty of ±15%.

Incident Momentum	u	Δu	dσ/du	Error
(GeV/c)	$(GeV/c)^2$	$(GeV/c)^2$	$\dfrac{nb}{(GeV/c)^2}$	$\dfrac{nb}{(GeV/c)^2}$
30.0	+0.004	0.008	225.2	53.1
	−0.010	0.020	172.5	33.2
	−0.035	0.030	125.4	27.4
	−0.070	0.040	124.2	29.3
	−0.110	0.040	111.2	30.9
	−0.155	0.050	85.0	24.5
	−0.210	0.060	86.9	22.4
	−0.285	0.090	53.6	15.5
	−0.380	0.100	33.2	13.6
	−0.480	0.100	< 23.4	
50.0	−0.004	0.013	55.8	13.6
	−0.025	0.030	62.7	11.4
	−0.060	0.040	60.0	11.2
	−0.105	0.050	49.9	11.8
	−0.160	0.060	30.2	8.6
	−0.240	0.100	10.7	4.3
	−0.340	0.100	6.0	3.5
	−0.440	0.100	3.1	3.1
70.0	−0.013	0.024	20.8	7.4
	−0.100	0.150	15.8	4.1
	−0.250	0.150	8.1	3.3
	−0.400	0.150	< 5.5	
90.0	−0.014	0.023	15.2	7.6
	−0.100	0.150	9.4	3.9
	−0.250	0.150	5.1	3.8
	−0.400	0.150	< 7.8	

TABLE 5.

Differential Cross Sections

$\pi^+ p \rightarrow p \pi^+$

Statistical errors only are listed; there is an additional overall normalization uncertainty of ±15%.

Incident Momentum	u	Δu	dσ/du	Error
(GeV/c)	$(GeV/c)^2$	$(GeV/c)^2$	$\dfrac{nb}{(GeV/c)^2}$	$\dfrac{nb}{(GeV/c)^2}$
30.0	+0.003	0.011	351.1	62.6
	−0.011	0.018	370.4	51.1
	−0.030	0.020	176.9	43.5
	−0.075	0.070	66.4	17.1
	−0.115	0.090	<12.3	
	−0.250	0.100	18.6	9.3
	−0.350	0.100	54.1	19.1
	−0.450	0.100	56.5	23.1
	−0.550	0.100	17.4	17.4
50.0	0.000	0.008	96.9	25.9
	−0.014	0.020	65.2	15.8
	−0.042	0.036	40.4	11.2
	−0.080	0.040	11.8	6.8
	−0.135	0.070	5.8	4.1
	−0.215	0.090	11.8	5.3
	−0.305	0.090	12.1	5.6
	−0.400	0.100	10.9	6.3
	−0.500	0.100	6.0	6.0
70.0	−0.011	0.018	26.6	9.7
	−0.045	0.050	12.2	5.1
	−0.120	0.100	< 4.4	
	−0.245	0.150	< 3.3	
	−0.395	0.150	< 6.3	

TABLE 6.

Exponential Fit of Backward Peaks

Incident Momentum	A	B
(GeV/c)	$\dfrac{nb}{(GeV/c)^2}$	$(GeV/c)^{-2}$
+30.0	333.8 ± 43.4	21.4 ± 3.8
+50.0	96.7 ± 18.9	24.3 ± 6.0
+70.0	36.8 ± 15.7	26.3 ± 13.1
-30.0	175.0 ± 20.0	4.37 ± 0.78
-50.0	73.2 ± 8.8	6.89 ± 0.92
-70.0	24.1 ± 6.6	4.71 ± 1.97
-90.0	16.1 ± 7.5	5.07 ± 4.01

FIGURE CAPTIONS

Figure 1   Pion-proton backward elastic scattering at 7.0 GeV/c; data from Baker et al.[8]

Figure 2   Baryon-exchange diagrams for pion-proton backward elastic scattering.

Figure 3   Fits to the $\pi^+ p$ data of Owen et al.[7] using the Regge model of Barger and Cline.[16]

Figure 4   a) $\pi^- p$ data at 38 GeV/c from Babaev et al,[23] together with a dashed line through the results of Owen et al[7] at 6 GeV/c. b) $d\sigma/du$ at u=0 for $\pi^+ p$. Data from Owen et al[7] (below 20 GeV/c) and Babaev et al[22] (above 20 GeV/c). The line is $P^{-2.7}$

Figure 5   Layout of the experiment for 30 and 50 GeV/c. W1-W11 represent groups of PWC's; S_{1-12}, F^a, F^b are scintillation counter hodoscopes. B_1, B_2, A are scintillation counters. Not shown are scintillation counters and a threshold Cerenkov counter in the incident beam upstream from the region shown in the Figure.

Figure 6   Schematic arrangement of the Fermilab M6 beam.

Figure 7   Backward spectrometer layout.

Figure 8   Simplified fast logic system.

Figure 9   Number of events as a function of x_π for 50 GeV/c $\pi^- p$ data. The shaded histogram shows the number of events after cuts on ΔPx, ΔPy and Δx_{W6}.

Figure 10   Number of events as a function of ΔP_x for 50 GeV/c $\pi^- p$ data. The shaded histogram shows the number of events after cuts on x_π, ΔP_y and Δx_{W6}.

Figure 11   Number of events as a function of ΔP_y for 50 GeV/c $\pi^- p$ data. The shaded histogram shows the number of events after cuts on x_π, ΔP_x and Δx_{W6}.

Figure 12   Number of events as a function of Δx_{46} for 50 GeV/c π^-p data. The shaded histogram shows the number of events after cuts on x_π, ΔP_x and ΔP_y.

Figure 13   Apparatus acceptance for 30 GeV/c data. Also shown as a dashed line is a $(\sin \theta_{lab}^\pi)^{-1}$ curve

which is the expected acceptance for a fixed vertical aperture at the S_{1-12} hodoscope.

Figure 14   Results of this experiment for the u-dependence of dσ/du for π^-p backward elastic scattering; upper error limits are 90% confidence. Solid lines are fits of the form Ae^{Bu} to the present data and those of Babaev et al.[23] Results of Owen et al[7] are represented by a dashed line.

Figure 15   Results of this experiment for the u-dependence of dσ/du for π^+p backward elastic scattering; upper error limits are 90% confidence. Solid lines are fits of the form Ae^{Bu} to the present data and those of Babaev et al.[22] Results of Baker et al[8] are represented by a dashed line. Remaining dashed lines are to guide the eye.

Figure 16   Results for B. Data are shown from this experiment and from References 4, 6-10, 12, 22, 23. The two lines shown are fits of the form $B = 2 \ln(P) + a$ constant to the data for each pion sign.

Figure 17   Results for dσ/du at u=0. Data are shown from this experiment and References 4, 6, 7, 8, 10, 12, 22, 23. The curves are the fits described in the text.

Figure 18   The effective trajectory for π^-p backward elastic scattering, derived as described in the text. The solid line is a linear fit to the data; the dashed line is the expected Δ_δ trajectory. a) Data from this experiment and References 4, 6, 7, 8. b) Data from this experiment only.

Figure 19   The effective trajectory for π^+p backward elastic scattering, derived as described in the text. The solid line is a linear fit to the data; the dashed line is the expected N_α trajectory. a) Data from this experiment and

References 4, 7, 8. b) Data from this experiment only.

Figure 20   Comparison between the 50 GeV/c $\pi^\pm$p data from this experiment and those predicted by the simple Regge model discussed in Reference 18 (solid lines).

Figure 21   Fits to the π^-p data of this experiment using the Regge model of Mir and Storrow.[35]

Figure 22   Fits to the π^+p data of this experiment using the Regge model of Mir and Storrow.[35]
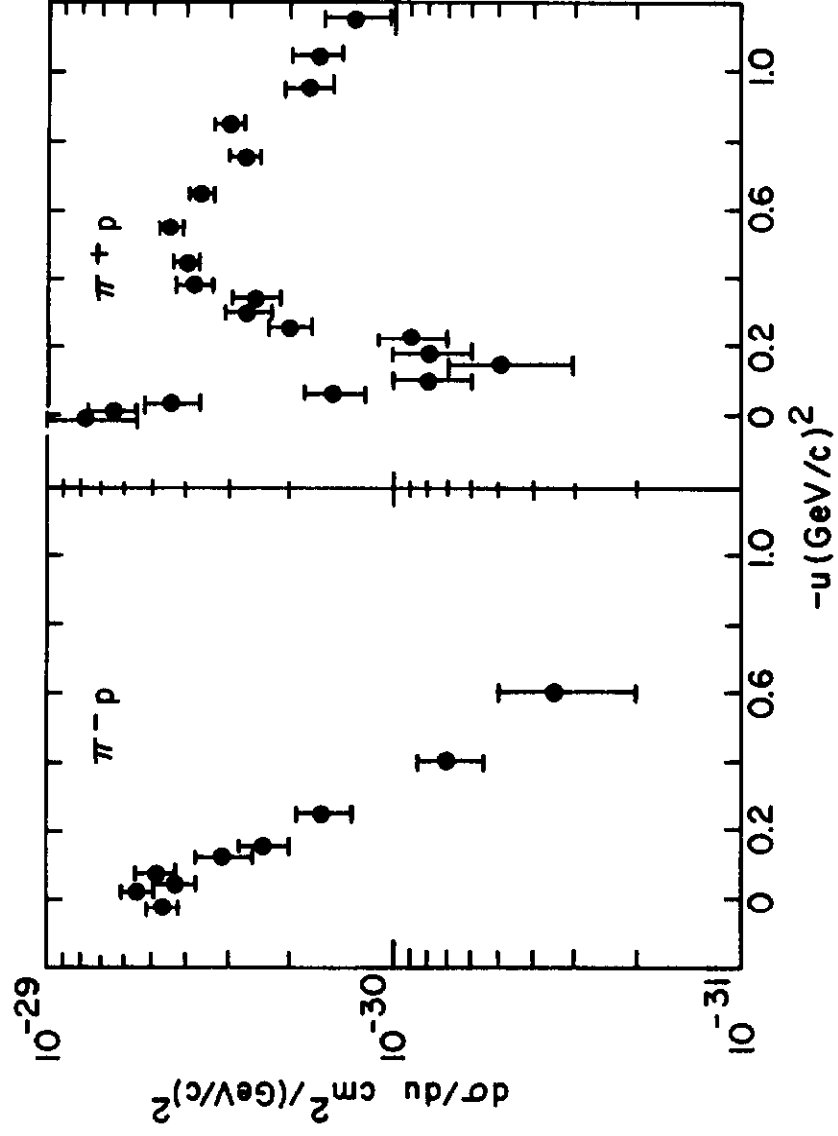
FIGURE 1
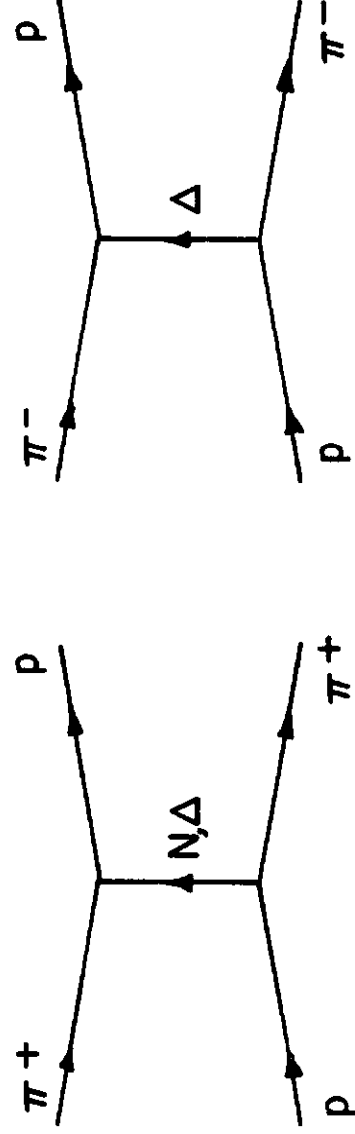
FIGURE 2
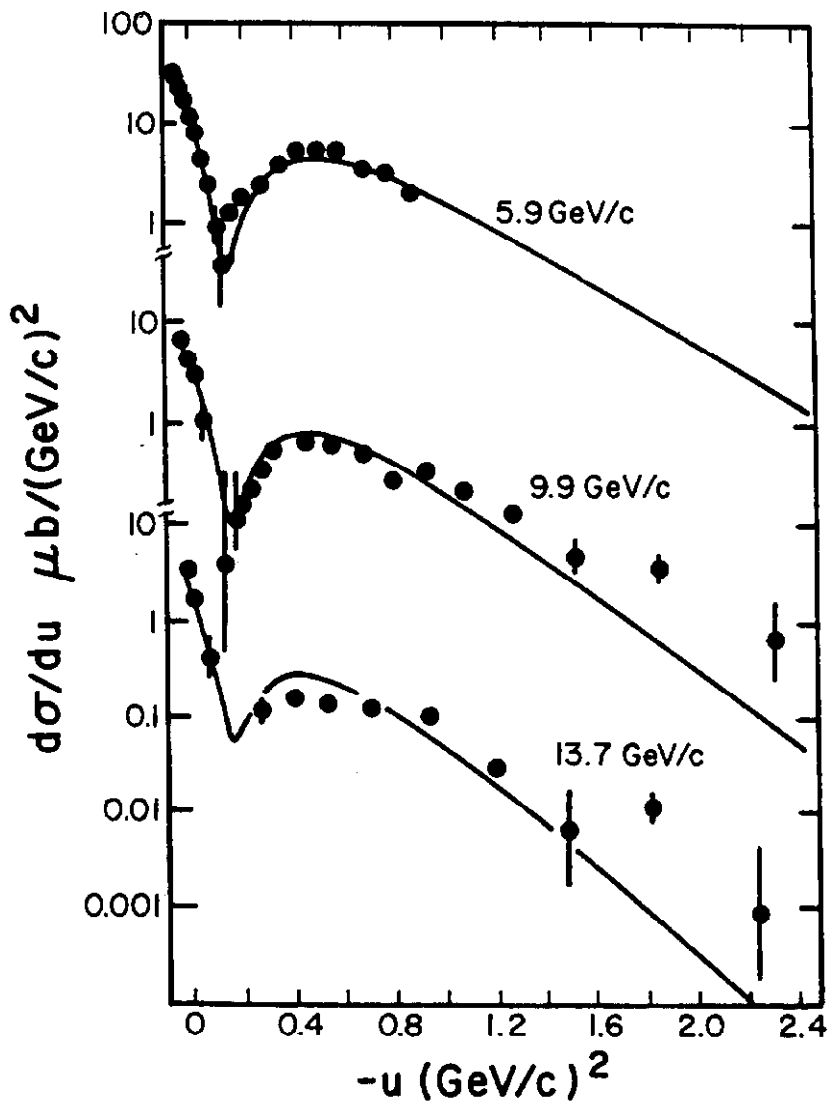
FIGURE 3
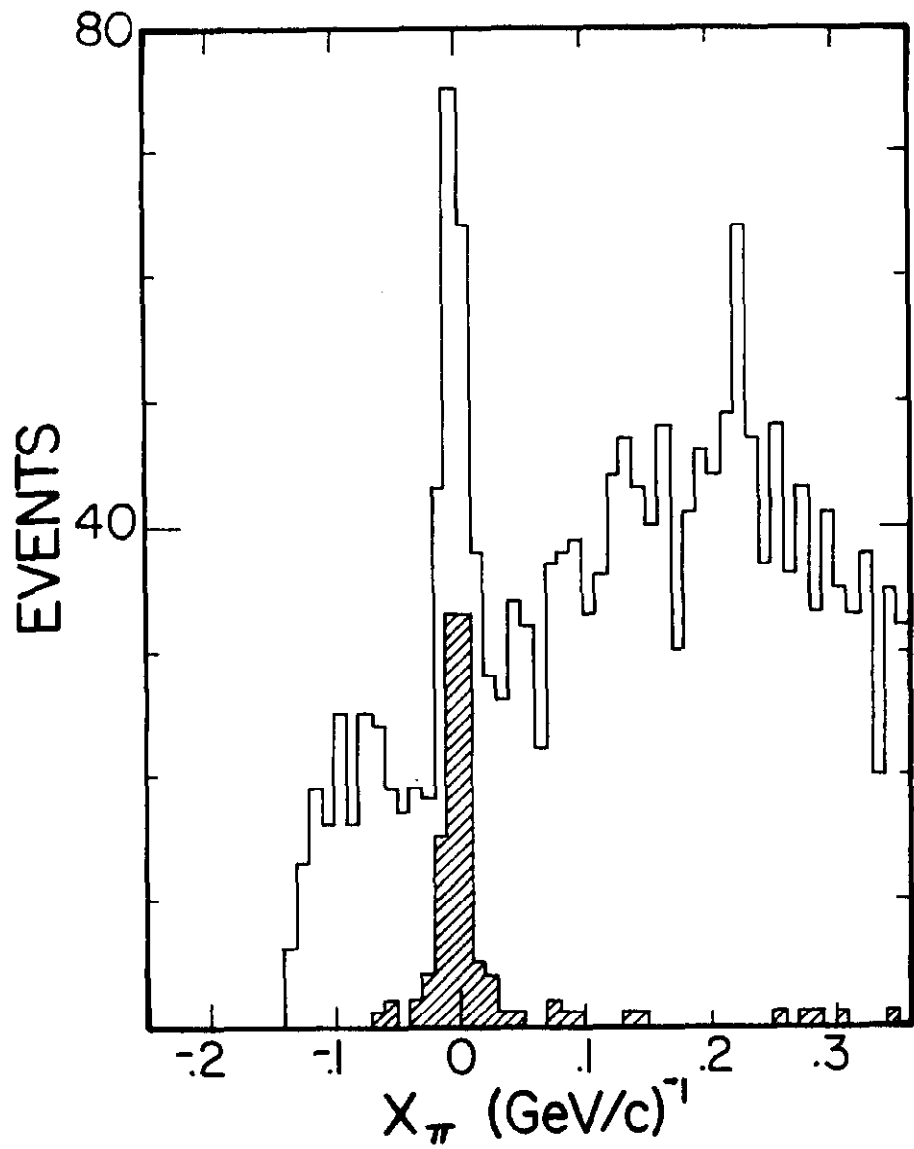
FIGURE 4

FIGURE 5

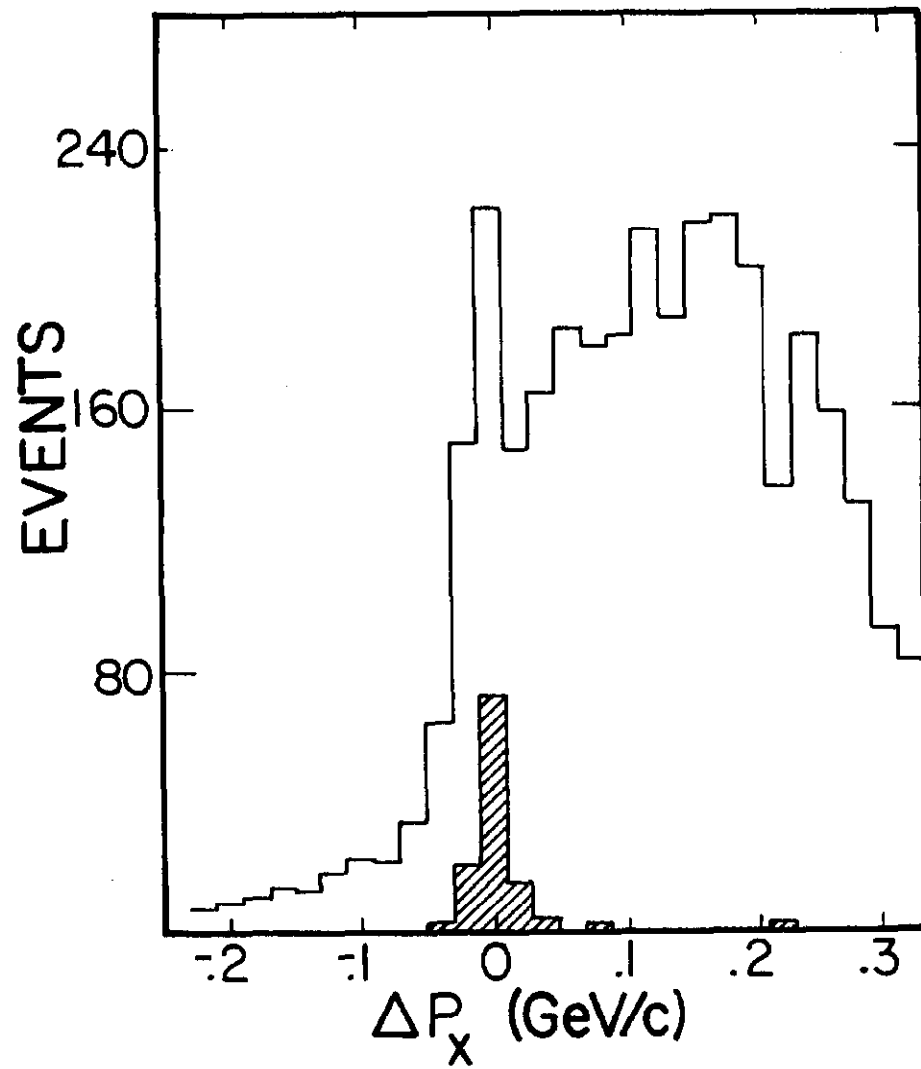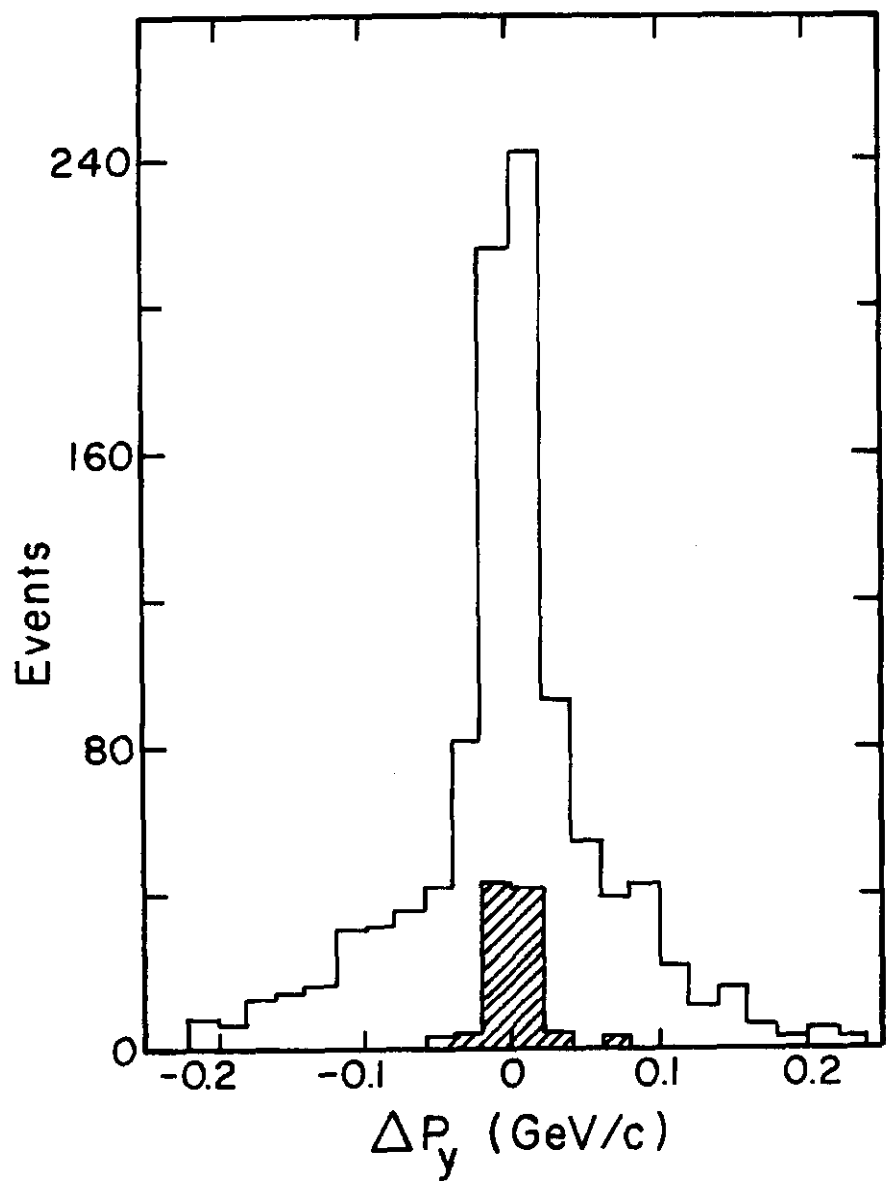EXTERNAL PROTON BEAM
BERYLLIUM TARGET
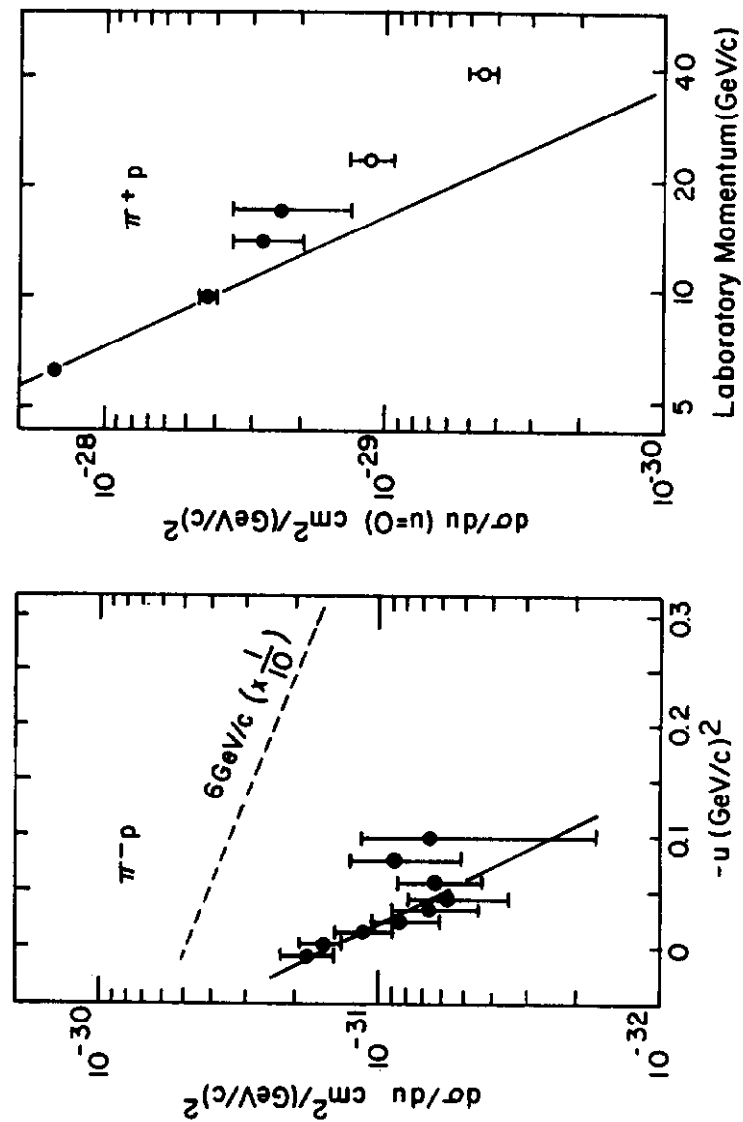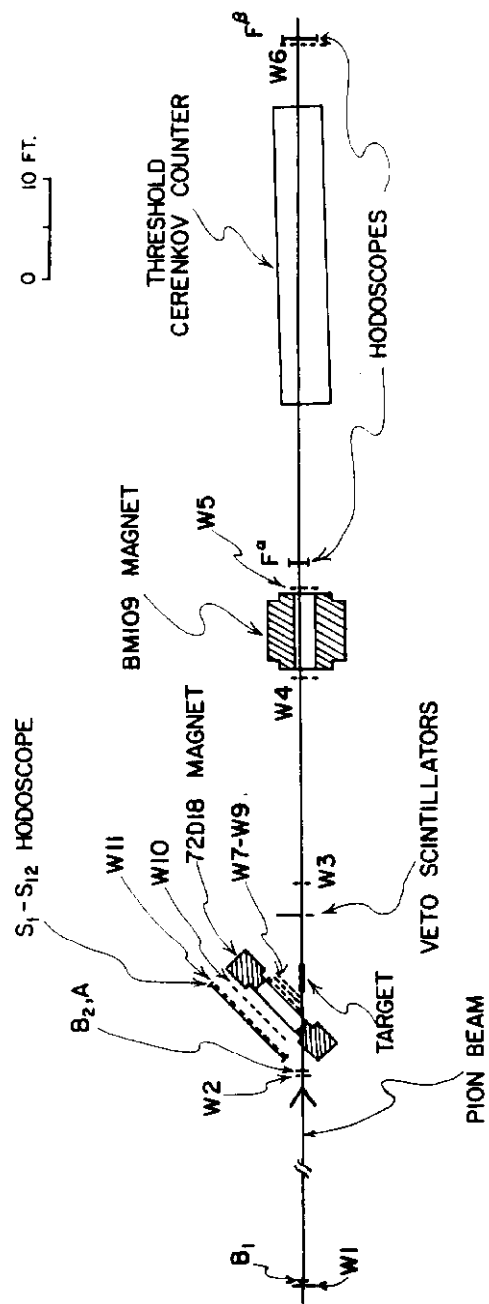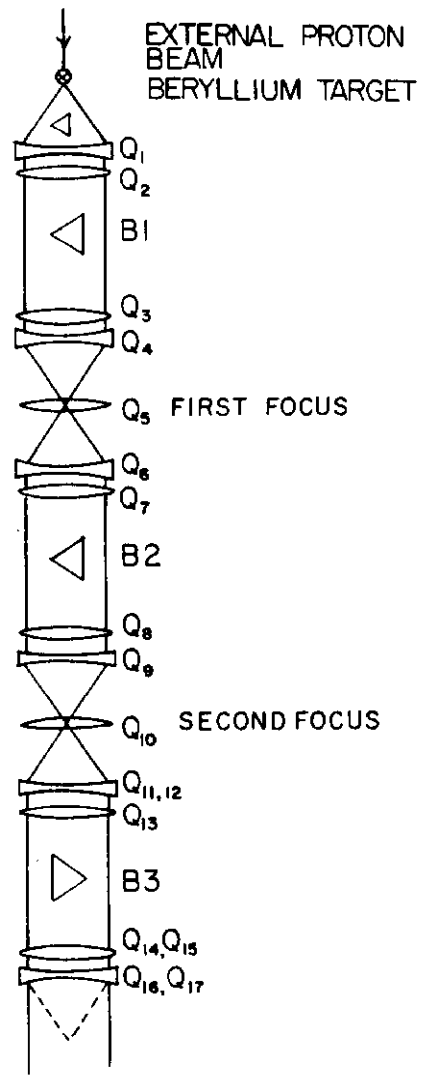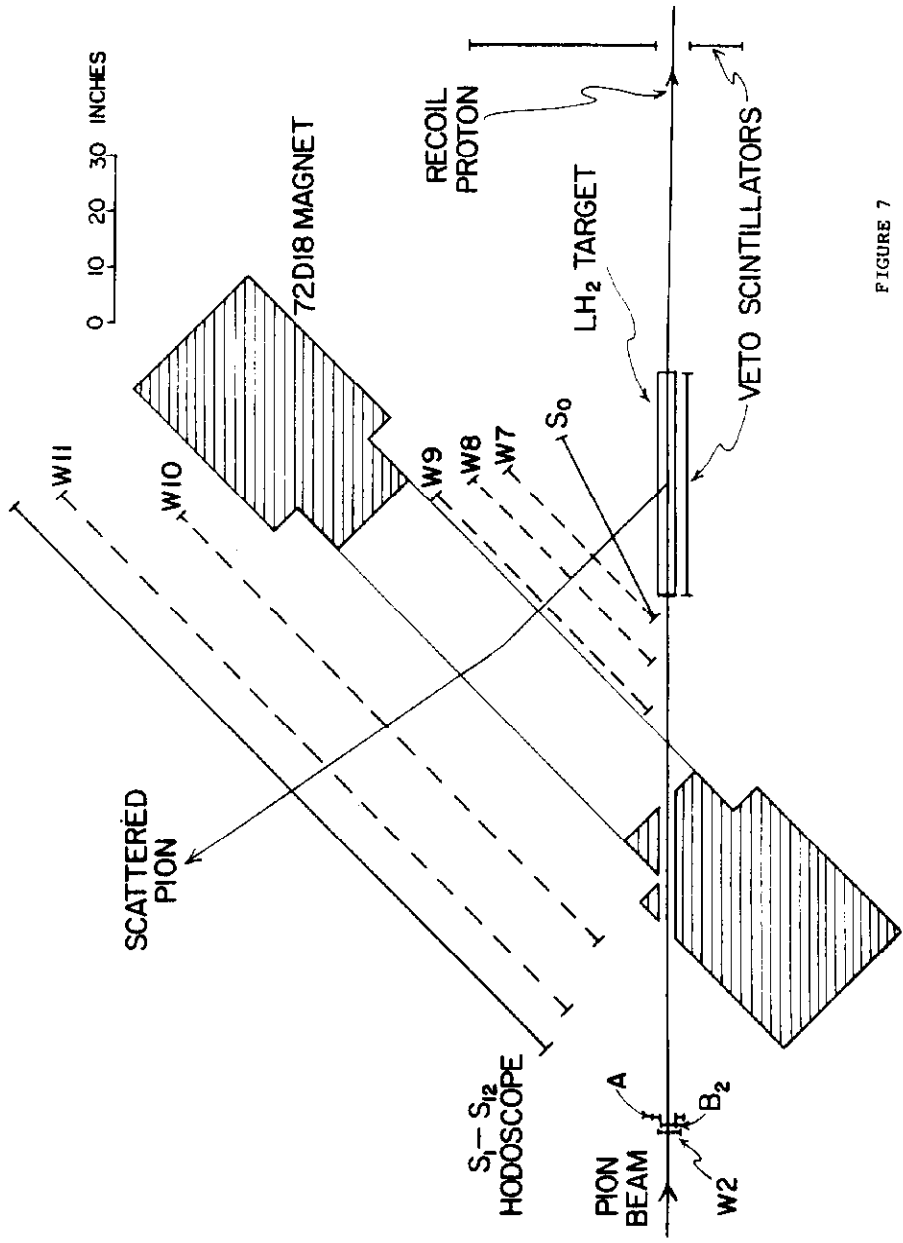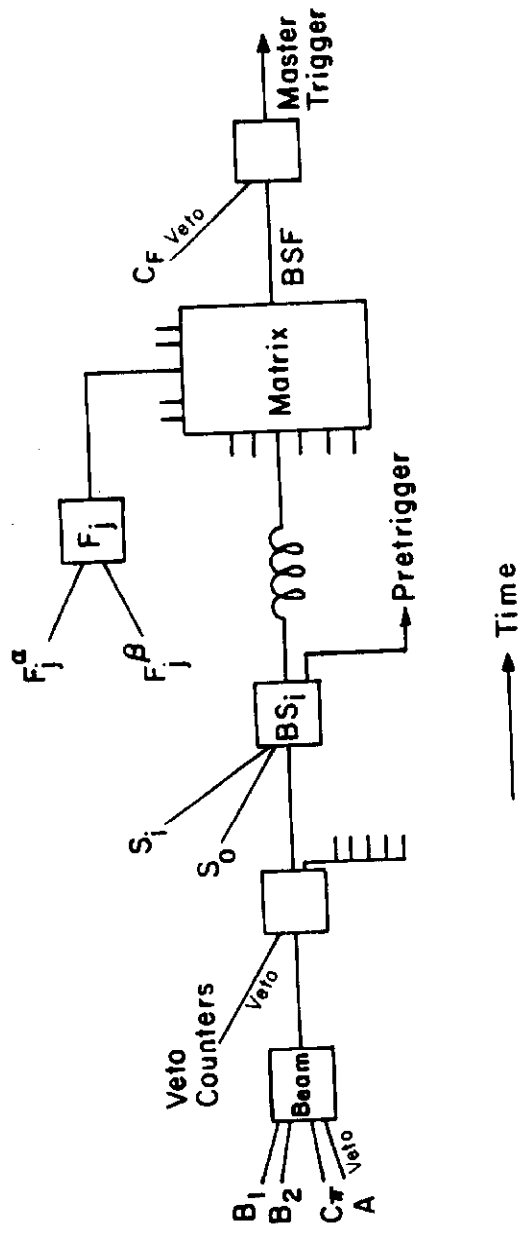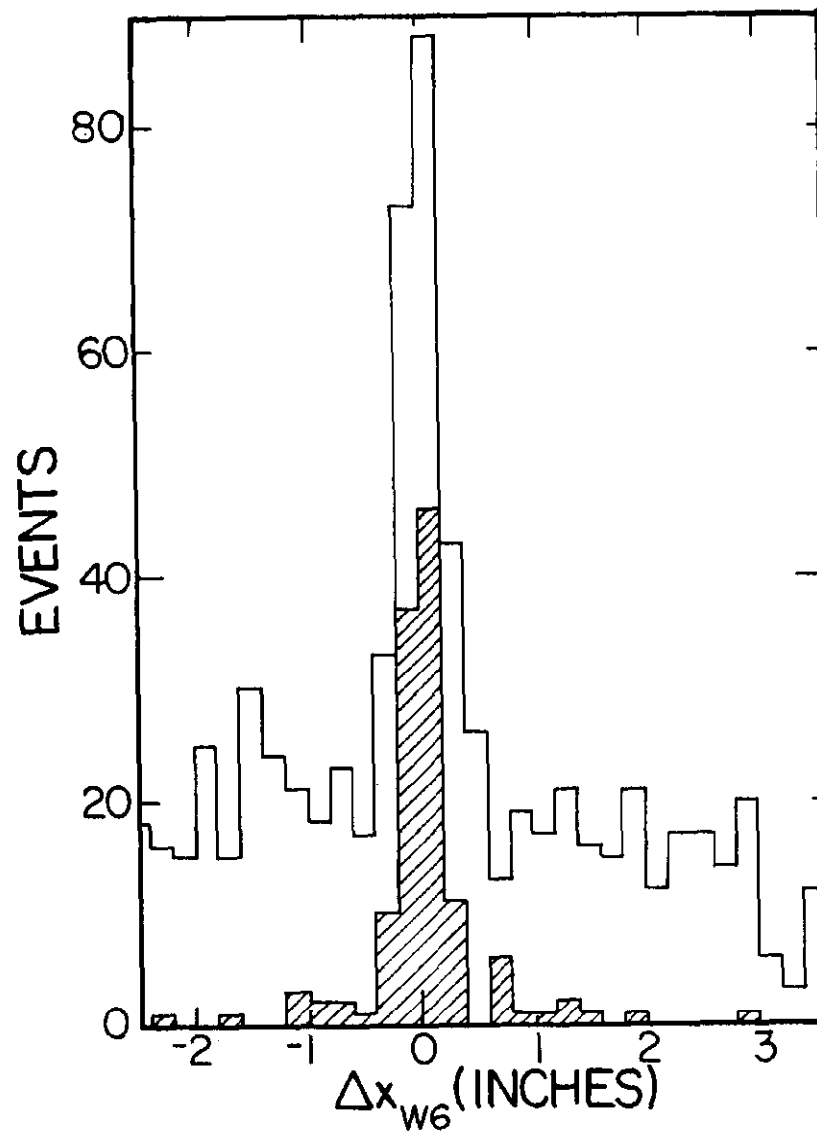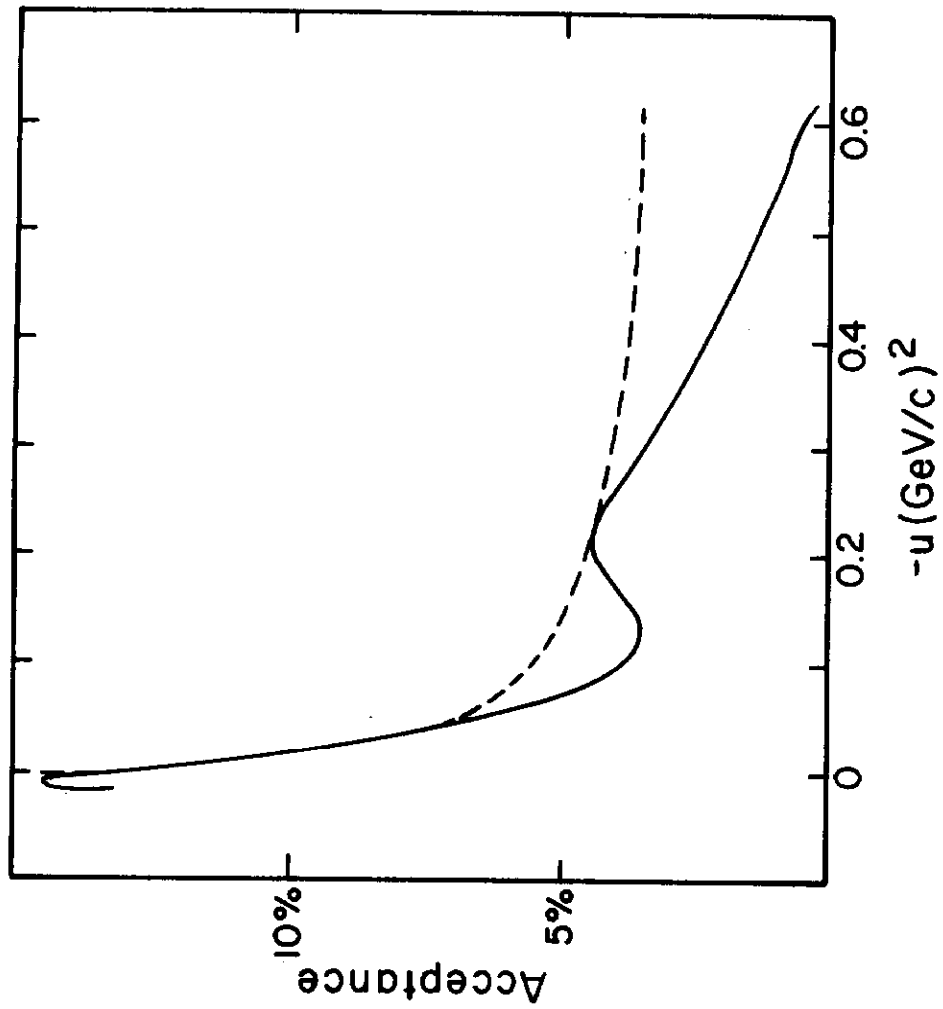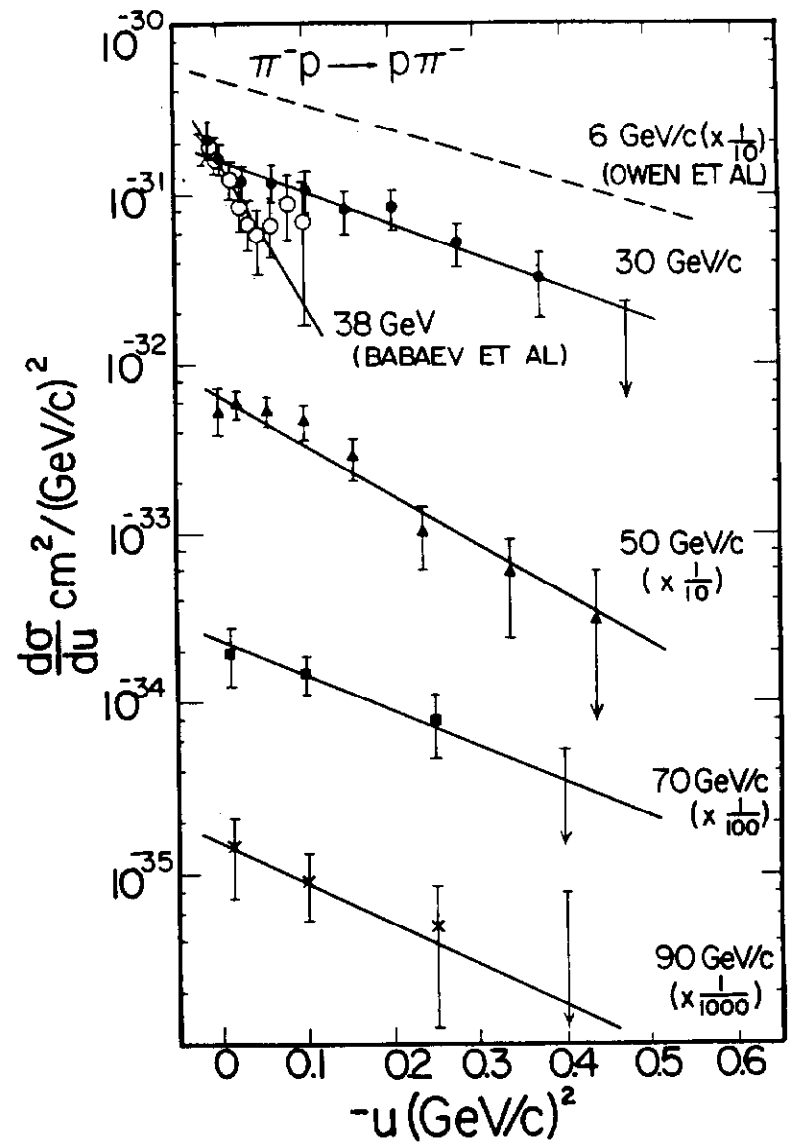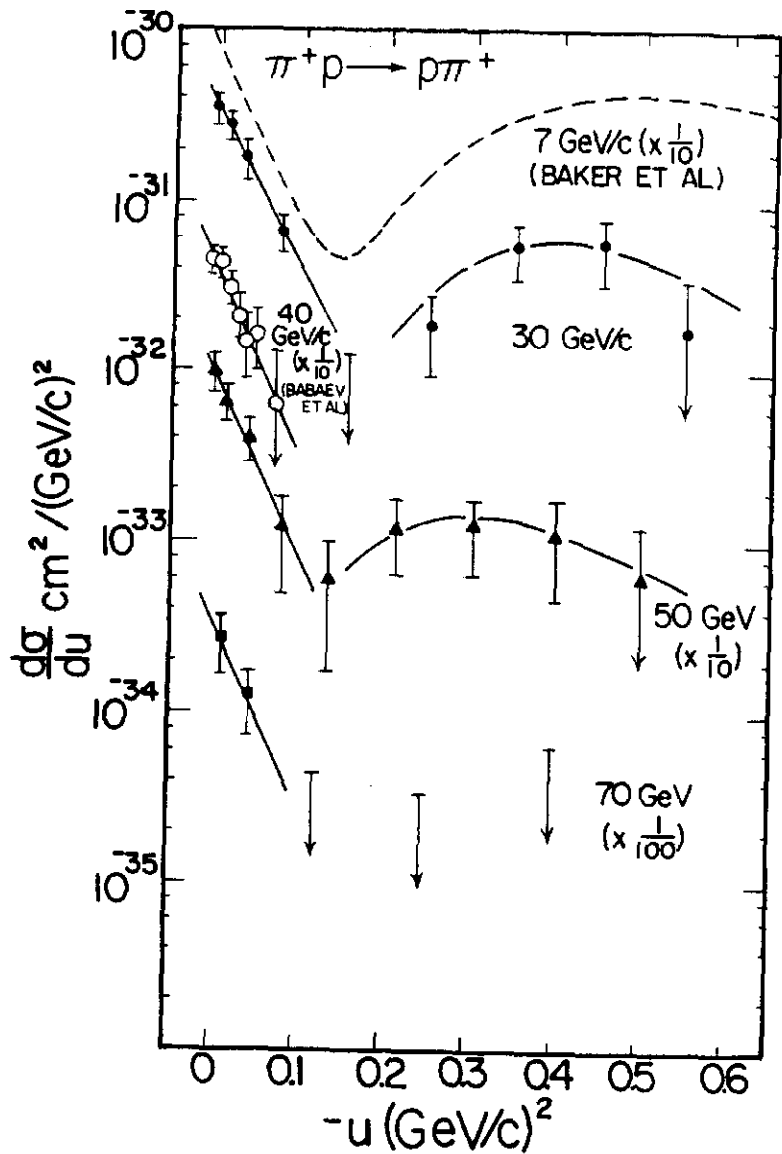
FIGURE 6

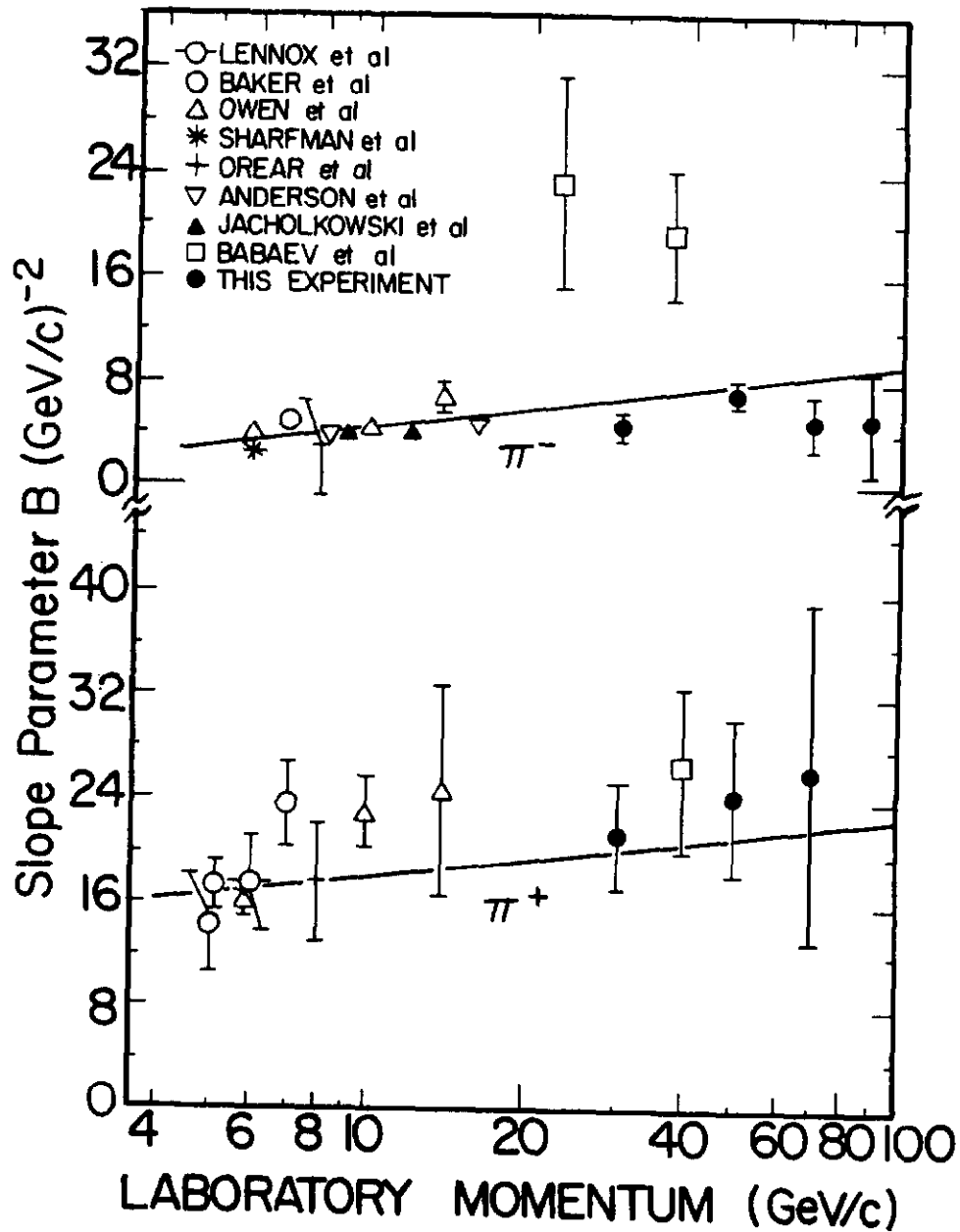FIGURE 7

FIGURE 8
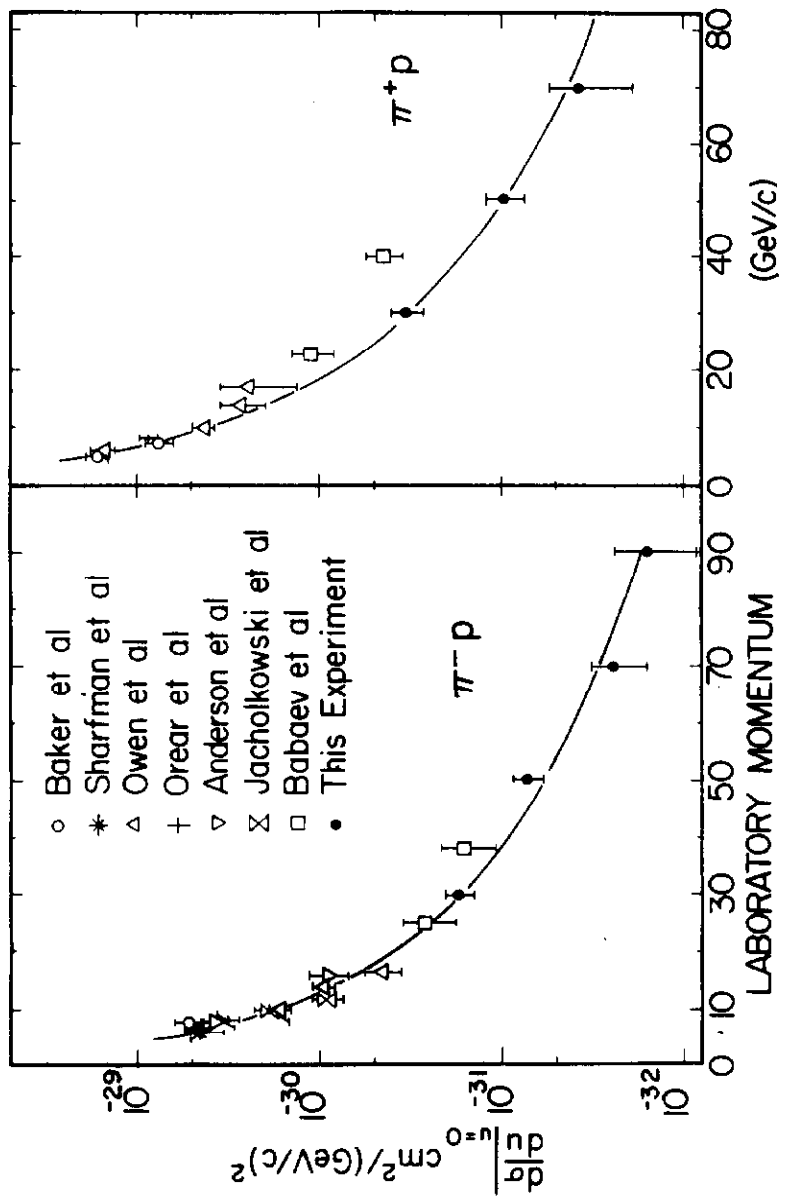
FIGURE 9
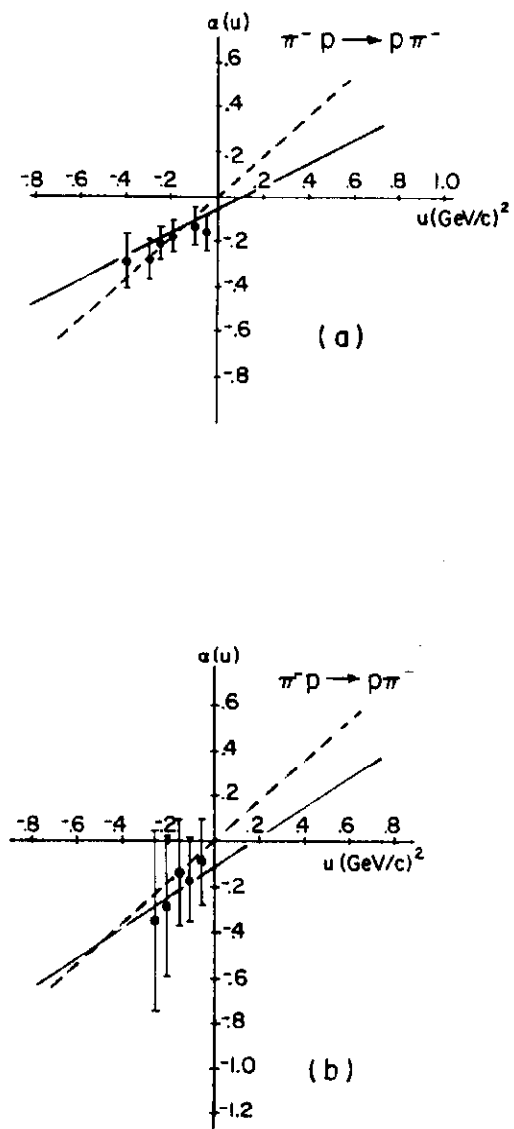
FIGURE 10
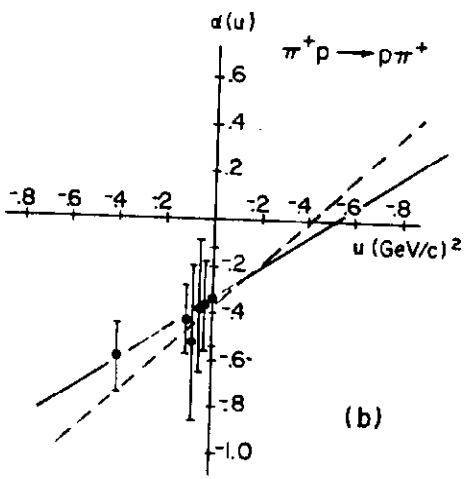
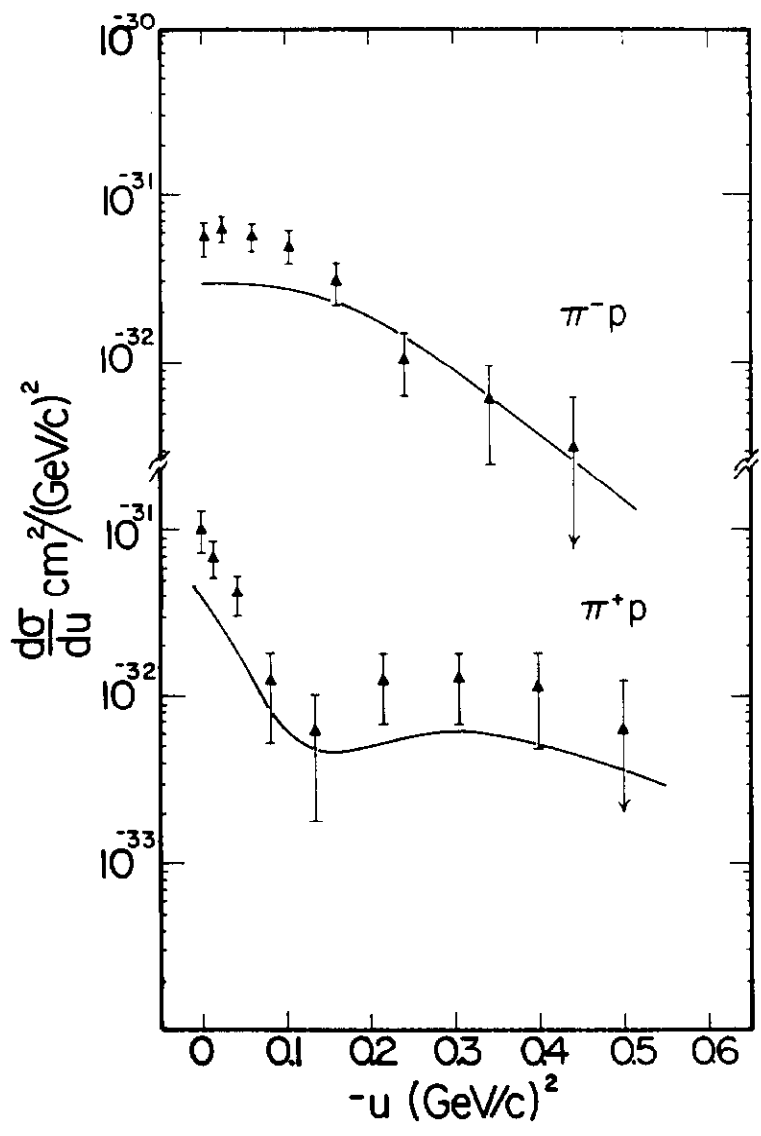FIGURE 11

FIGURE 12

FIGURE 13

FIGURE 14

FIGURE 15

FIGURE 16

FIGURE 17

FIGURE 18
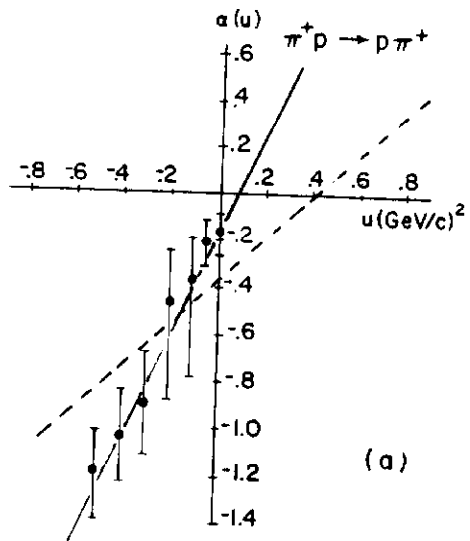
FIGURE 19

FIGURE 20

FIGURE 21

FIGURE 22